

LoC-Path: Learning to Compress for Pathology Multimodal Large Language Models

Qingqiao Hu¹ Weimin Lyu¹ Meilong Xu¹ Kehan Qi¹
 Xiaoling Hu² Saumya Gupta¹ Jiawei Zhou¹ Chao Chen¹

¹Stony Brook University, Stony Brook, NY, USA

²Harvard Medical School, Boston, MA, USA

qingqiao.hu@stonybrook.edu

Abstract

Whole Slide Image (WSI) understanding is fundamentally challenging due to its gigapixel scale and extreme sparsity of diagnostically relevant regions. Unlike human experts who primarily rely on key areas to arrive at the diagnosis, existing slide-level multimodal large language models (MLLMs) for pathology rely on heavy slide-level encoders that process thousands of tile/patch features in a brute-force manner, resulting in excessive computational cost. In this work, we revisit the WSI-language modeling paradigm and reveal that tile-level features exhibit strong global and local redundancy, whereas only a small subset of informative tiles are truly task-relevant. Motivated by these observations, we introduce an efficient MLLM framework, called LoC-Path, that replaces the expensive slide-level encoder with redundancy-reducing modules. We first design a Sparse Token Merger (STM) and an MAE-pretrained resampler to remove local redundancy and compress globally redundant tile tokens into a compact slide-level representation set. We then propose a Cross-Attention Routing Adapter (CARA) and a Token Importance Scorer (TIS) to integrate the compressed visual representation with the language model in a computation-efficient manner. Extensive experiments demonstrate that our approach achieves performance comparable to existing state-of-the-art whole slide MLLMs, but with significantly lower computational and memory burden.

1. Introduction

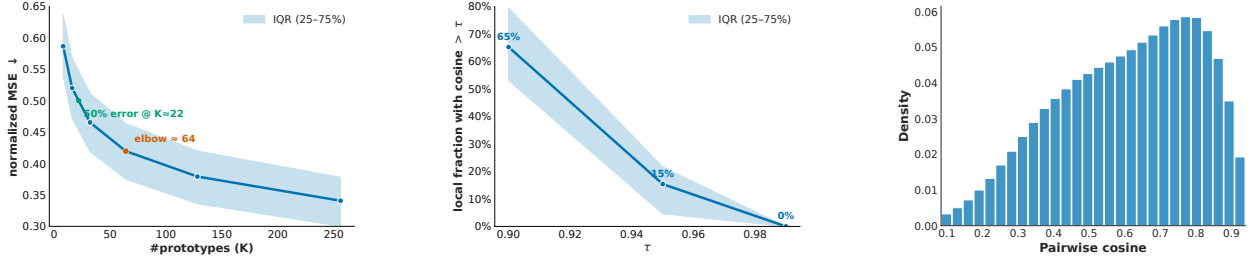
Digital pathology has undergone a significant revolution in recent years. Whole Slide Images (WSIs), with many exceeding $10,000 \times 10,000$ pixels, are partitioned into small

patches.¹ Powerful pretrained image encoders [7, 32, 48] are applied to these patches to extract patch-wise features. These features are then aggregated through an attention mechanism to make a whole-slide level prediction [24, 29, 55], whereas the attention will highlight a potentially small set of critical patches, imitating how pathologists make clinical decisions.

The advent of large language models (LLMs) has further changed the WSI prediction methodology. Given whole slide images, new LLM-based methods can not only make predictions such as subtype classification or survival prediction, but also generate content-rich text-based outputs, including answers to questions (VQA) or pathology reports. In particular, adapting recent multimodal large language models (MLLMs) [1, 26, 28], methods such as WSI-LLaVA [27], SlideChat [9], TCP-LLaVA [35], and AL-PaCA [15] process features of all patches with a vision encoder to convert them into visual tokens, and then concatenate these visual tokens with language tokens (from a question or other textual information) as a long sequence and send it to pretrained LLMs.

Despite the strong prediction and generation power, these LLM-based methods all suffer from an efficiency issue. Due to the large size of a whole slide image, there can be thousands of patches, resulting in thousands of tokens being fed to an LLM. Even with a frozen LLM backbone, the extensive forward and backward passes over thousands of tokens represent a massive computational bottleneck, resulting in prolonged training durations for fine-tuning a 7B model. Furthermore, before sending these visual tokens into LLMs, it is often necessary to improve their representation quality through global reasoning, e.g., using attentional poolers to summarize slide-level features as additional features [14] or using LongNet [13] to capture the diagnostically relevant global dependencies [52] efficiently.

¹Throughout this paper, we use *tile* and *patch* interchangeably.



(a) **Compression.** Mean normalized reconstruction error vs. K ; shaded band shows interquartile range across slides. We mark the elbow and the K needed to reach 50% reconstruction error.

(b) **Local redundancy.** Fraction of tiles whose nearest neighbor exceeds cosine threshold τ ; IQR across slides. Values above each dot indicate the mean fraction.

(c) **Pairwise similarity.** Aggregated cosine histogram with vertical lines at the τ used in (b); annotations report $P(\cos > \tau)$. The inset zooms into the high-similarity tail.

Figure 1. **WSI tile tokens are redundant globally and locally.** We analyze $\sim 2k$ TCGA WSIs (tissue tiles at $20\times$; features from CONCH-V1 [32]). We showed that (a) we only need a small number of prototypes to reconstruct all tokens; (b) locally, tokens are similar to each other; and (c) globally, tokens are also similar.

Although these models are capable of capturing the global context, reasoning over thousands of visual tokens creates a substantial computational and memory burden on the vision side.

To address these efficiency limitations, we initiate a quantitative investigation to answer *a fundamental question: are these thousands of tokens really necessary?* The answer, we find, is “no”, for two key reasons.

Reason 1: redundancy of token content. We observe that the tile-level token sequences of WSIs are highly redundant both *globally* and *locally*. We analyze the tile features of the 2,000 TCGA [50] WSIs and show in Fig. 1: (1) a small set of $K \approx 250$ prototype groups can fairly well reconstruct the entire tile feature set; and (2) tile features are highly similar to each other, as observed by comparing neighboring tiles and comparing pairs of tiles far apart. These findings confirm strong redundancy in both global content and local neighborhoods, suggesting that WSIs can be effectively represented by a compact set of latent representations rather than the full sequences of thousands of tokens.

Reason 2: irrelevance to the task. We also observe that only a limited number of tiles are truly relevant to the task, i.e., relevant to the text supervision (answers in the VQA task, and report content in the report generation task). We use the same 2,000 TCGA WSIs and compute the cosine similarity between each tile token and the corresponding text supervision embedding. We rank tokens by their descending cosine similarity with the text supervision and compute the cumulative sum of positive similarity as a function of total token fraction. Shown in Fig. 2, the top 35.2% of tile tokens account for 90% of the total cosine similarity. In other words, a majority of visual tokens are irrelevant to the pathology report. This aligns with the fact that human experts only rely on key areas of WSIs for diagnosis. More analysis details are in Sec. 6.

Our contribution. Inspired by these observations, we tackle the efficiency of pathology MLLMs. Focusing on the

two issues, we propose an efficient framework named **LoC-Path** with novel modules to (1) reduce the token redundancy, and (2) select only task-relevant tokens for the pre-trained LLM. As a consequence, we reduce the number of tokens sent to LLMs from thousands per slide to hundreds, decrease inference computation by 70%, and reduce memory consumption by 30% without sacrificing much prediction/generation power.

To reduce *global redundancy* of tokens, we design a lightweight **resampler** inspired by how pathologists inspect WSIs. The resampler scans all the tile-level tokens and then selects those crucial ones for reconstructing the whole slide with a set of learnable queries. This transforms thousands of redundant tile tokens into a compact set. To teach the resampler how to *glance broadly and select distinctively*, we adopt Masked Autoencoder (MAE) pre-training [18], which encourages recovery of missing tiles from partial observations. Compared to conventional slide-level encoders, our resampler is light-weight, significantly improving computational efficiency. Furthermore, to reduce *local redundancy*, we introduce a sliding-window Sparse Token Merger (**STM**) that merges highly correlated neighboring tiles before resampling, reducing sequence length while preserving representative tissue diversity.

To select task-relevant tokens, we propose a novel Token Importance Scorer (**TIS**) module to select tokens that are the most relevant to the task. Using query text token information, TIS ranks the projected visual tokens and selects the top- M most relevant ones. Furthermore, existing LLaVA-style fusion methods use self-attention on concatenated visual and text tokens [28]. We stipulate that this is unnecessary, and propose to use cross-attention across visual and text tokens instead. Assuming n visual tokens and n textural tokens, the self-attention will generate $(2n)^2 = 4n^2$ attention values, whereas cross-attention will only generate n^2 attention values, saving computation by 75%. We inject TIS-selected visual tokens into multiple decoder lay-

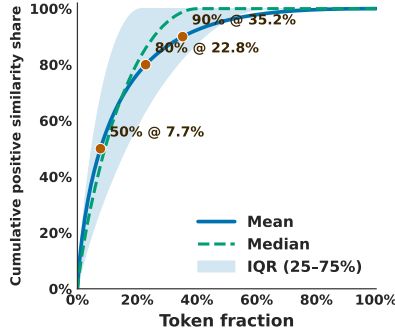


Figure 2. **Most tokens are not task-relevant.** For each slide, we sort tokens by their cosine similarity to the slide caption (expert report) and compute the cumulative share of positive similarity as a function of the token fraction. We report the mean (solid), median (dashed), and inter-quartile range (shaded) over different slides. Reaching 50%, 80%, and 90% of the positive similarity mass requires $\approx 7.7\%$, $\approx 22.8\%$, and $\approx 35.2\%$ of tokens, respectively. This shows that a small subset of tokens carries most report-relevant information.

ers of the LLM through Cross-Attention Routing Adapters (**CARA**) equipped with learnable gating mechanisms. This multi-layer routing allows richer supervision from multiple depths of the LLM, improving alignment while also reducing computation due to the aforementioned reason.

In summary, our main contributions are as follows.

- **WSI token compression.** Inspired by the observed high global and local redundancy of WSI tile tokens, we propose a lightweight, MAE-pretraining-based **resampler** to eliminate global redundancy. We also propose an **STM** to eliminate local redundancy.
- **Efficient visual token selection and multimodal fusion.** We introduce **TIS** module that selects the most task-relevant tokens, and integrates these tokens with the pre-trained LLM through gated cross-attention and dynamic token routing (**CARA**), yielding much lower computational complexity than standard LLaVA-style fusion.
- **Efficiency with competitive performance.** On different benchmarks, our *LoC-Path* framework achieves comparable or superior performance compared to SOTA WSI MLLMs, while significantly reducing computation and GPU memory consumption.

2. Related Work

Multimodel Large Language Models (MLLMs) for Digital Pathology. The development of multimodal large language models (MLLMs) has revolutionized computational pathology by enabling sophisticated integration of visual and textual information for histopathological analysis [4, 25]. Recent work has introduced specialized vision-language models for pathology that combine pretrained vision encoders with large language models through instruc-

tion tuning on extensive pathology datasets, achieving state-of-the-art performance on diagnostic tasks [23, 30, 34]. Advanced systems leverage contrastive learning frameworks trained on large-scale image-caption pairs to develop foundation models capable of zero-shot transfer across diverse histopathological tasks [31, 33]. Comprehensive benchmarking studies have systematically evaluated foundation models across multiple pathology datasets, revealing that pathology-specific vision-language models consistently outperform general-purpose vision models on histopathological tasks [3, 16]. Recent efforts have extended these capabilities to whole-slide image understanding, enabling multimodal reasoning at the slide level through specialized architectures that process gigapixel images with clinical context [9, 27, 36, 44, 45].

Token Reduction in MLLMs: Resamplers and Compression.

A central obstacle for MLLMs is the quadratic cost of attention with long visual sequences. Recent work reduces the effective number of visual tokens via three routes. *(i) Architectural bottlenecks / resamplers.* A fixed-length latent interface distills variable-length vision streams before they reach the LLM. Flamingo uses a Perceiver-style resampler to map dense image/video features into a short latent set consumed by gated cross-attention [1]; BLIP-2 adopts a text-guided Q-Former that queries a frozen vision encoder and exposes only a few language-relevant latents [26]. More recent open models follow a similar principle: MiniCPM-V introduces a unified 3D-Resampler that compresses multi-frame inputs (up to $\sim 96\times$ video token reduction) while maintaining accuracy [54]; Qwen2-VL couples a dynamic-resolution visual front-end with M-ROPE to produce variable token budgets that better match input scale [49]. These resamplers are often trained alongside the LLM itself with millions of vision language pairs. Such data scale is scarce in the digital pathology domain. Therefore, we adopt MAE pretraining for our resampler under a digital pathology context. *(ii) Token compression inside the VIT.* Training-free and training-based methods directly thin out visual tokens before they ever reach the LLM. Token Merge merges tokens before LLM [5, 56] divides visual tokens to two parts and merges them according to the link in a bipartite graph. LLaVA-PruMerge [42] selects high-score tokens and merges the rest by key-similarity clustering. DivPrune [2] prunes the visual tokens that are not similar according to the pairwise cosine similarity. Our **STM** belongs to this family: it performs sliding-window merging on 2D grid, eliminating obvious local redundancy while preserving coarse spatial layout. *(iii) Token compression inside the LLM.* A third route reduces cost within the LLM. FastV prunes deep-layer tokens in a plug-and-play manner to achieve large FLOPs savings with minimal degradation [6]; FitPrune formulates pruning as matching attention statistics to derive a per-layer recipe within min-

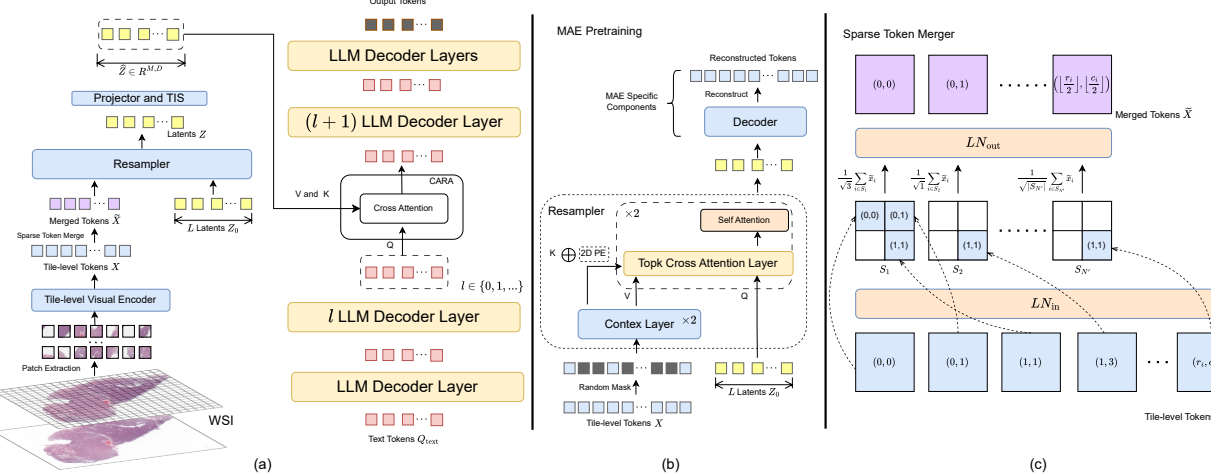


Figure 3. The overall framework architecture of *LoC-Path*, MAE pretraining for Resampler, and the computational illustration of STM. (a) Foreground tile tokens, \mathbf{X} , are generated by the tile-level vision encoder. STM merges them to $\hat{\mathbf{X}}$. Then the resampler takes both $\hat{\mathbf{X}}$ and learnable latents \mathbf{Z}_0 as input. The projector aligns the embedding dimension of output latent \mathbf{Z} with LLM’s hidden dimension, D . The scorer selects the top M latents, $\hat{\mathbf{Z}}$ among L latents, where $M \leq L$. The CARA modules are inserted into multiple LLM decoder layers. Within each adapter, the latents perform cross-attention with the hidden state of LLM. (b) Resampler is pretrained *without* STM. The tile-level tokens, \mathbf{X} are first randomly masked and then sent to context layers. Outputs, $\hat{\mathbf{X}}$ from context layers serves as \mathbf{V} and \mathbf{K} for the following cross-attention layers; a 2D positional encoding (PE) is added only to \mathbf{K} . During pre-training, a two-layer decoder is used to reconstruct the tokens from the resampler’s output latents. (c) The diagram shows the merging process when window size $s = 2$. White blocks indicate empty positions (zero tokens) in \mathcal{S}_g . The LN_{in} and LN_{out} are applied per tile token along the feature dimension D_v .

utes [53]. Beyond the prefill stage, Dynamic-LLaVA sparsifies both vision *and* language contexts to sustain end-to-end speedups during decoding [20]. PACT mixes pruning with k-means-style clustering to remove irrelevant tokens while merging redundant ones, sustaining higher reduction ratios with smaller accuracy loss [12]. Our **CARA+TIS** avoids concatenating visual tokens with query tokens, which differs from previous methods: it performs cross-modal fusion by dynamically selecting only the Top- M most salient latents into a few decoder layers via gated cross-attention. The speedups extend beyond prefill as decoding steps only attend to M latents.

3. Methodology

A WSI is decomposed into a long sequence of tiles. For each training image-text pair, we denote the tile-level tokens from the tile-level encoder by $\mathbf{X} = [\mathbf{x}_1, \dots, \mathbf{x}_N] \in \mathbb{R}^{N \times D_v}$, with 2D-grid coordinates $\mathbf{C} = (c_i, r_i) \in \mathbb{N}^2$, where N is the number of the tile-level tokens, D_v is the tile-level encoder’s feature dimension. c_i and r_i are the column and row grid coordinates with stride 1, respectively. In MAE pre-training task, we produce L -length visual latents $\mathbf{Z} \in \mathbb{R}^{L \times D'_v}$, where D'_v is the embedding dimension of MAE resampler. The text query tokens are \mathbf{Q}_{text} and the answer labels are \mathbf{Y} . In single-round visual question answering (VQA) tasks, $\hat{\mathbf{Y}}$ is generated by an MLLM for a given \mathbf{X} and text query \mathbf{Q}_{text} .

Overview. Our **LoC-Path** framework is illustrated in

Fig. 3. During inference, tile-level tokens, \mathbf{X} are merged by STM to $\hat{\mathbf{X}}$. MAE-pretrained resampler compresses the merged tokens $\hat{\mathbf{X}}$ to latents $\mathbf{Z}_0 \in \mathbb{R}^{L \times D'_v}$. The projector converts the embedding dimension and TIS selects Top- M latents, $\hat{\mathbf{Z}}$. The selected $\hat{\mathbf{Z}}$ are integrated with LLM’s multiple decoder layers through CARA modules.

3.1. Compressing Slide-level Representation

To achieve a concise yet informative slide-level representation, we emulate the way human pathologists examine WSIs in our resampler design. To teach the resampler to achieve this goal, MAE pre-training is adopted: the resampler is forced to scan the whole tile-level sequence and select the tokens that are crucial for reconstruction.

Resampler for Tile-level Token Compression. To compress the tile-level tokens, we adopted the popular resampler-style design in many open-source MLLMs [1, 49, 54]. Unlike the previous designs, we break down our design into two parts: scanning and selecting to imitate human experts. A set of context layers scans the whole tile-level sequence roughly, just like the human scanning WSIs. After scanning, we design a set of learnable latent queries, each latent selects the distinct tile-level tokens from WSI. To make each latent work separately instead of looking at the same area, a Top-K attention forces each latent to look at the input token that has Top- K attention scores. Then a self-attention module allows each latent to interact with each other to prevent them from looking at the same set of to-

kens. The details of the resampler architecture are shown in Fig. 3 (b). Concretely, given tile-level tokens $\mathbf{X} \in \mathbb{R}^{N \times D_v}$, we first apply a set of lightweight context layers to obtain $\hat{\mathbf{X}} = \text{ContextLayers}(\mathbf{X})$, where $\hat{\mathbf{X}} \in \mathbb{R}^{N \times D_v}$. Then initial L learnable queries $\mathbf{Z}_0 \in \mathbb{R}^{L \times D'_v}$ attend to $\hat{\mathbf{X}}$ through R stacked Top-K cross-attention blocks with a LayerNorm and a residual FFN. We inject 2D positional encoding only on **key**: $K = (\hat{\mathbf{X}} + \Phi)W_k$, $V = \hat{\mathbf{X}}W_v$. For each block: $\mathbf{H} = \text{softmax}(\text{TopK}(\text{LN}(\mathbf{Z}_{\ell-1})K^\top/\sqrt{d_h}))V$, $\mathbf{Z}'_\ell = \mathbf{Z}_{\ell-1} + \mathbf{H}$, $\mathbf{Z}''_\ell = \mathbf{Z}'_\ell + \text{FFN}(\text{LN}(\mathbf{Z}'_\ell))$. A self-attention layer following the cross-attention layer further decorrelates latents. TopK keeps the largest K_{top} entries per head and per query (others set to $-\infty$ before softmax). The final output from the resampler is the latents, $\mathbf{Z} \in \mathbb{R}^{L, D'_v}$, where $L \ll N$.

MAE Pre-training for Redundant Tile-level Tokens. Humans only require hundreds of WSIs to learn how to find diagnoses. Sadly, it does not hold for machines. To teach the resampler with a limited number of available WSIs (around 30k WSIs in the TCGA dataset [50]), we adopt the Masked Auto-encoder pre-training framework. As we have shown in Fig. 1a, the highly redundant tokens mean that the resampler can reconstruct masked tiles from visible context without overfitting to noise. Moreover, reconstruction on randomly masked indices prevents the resampler from outputting trivial averages and forces different latents to look at complementary regions. Concretely, we add a small decoder to use the latents for reconstruction, shown in Fig. 3 (b). The pre-training objective is written as: $\mathcal{L}_{\text{rec}} = \frac{1}{|N|} \sum_{i \in N} \|\hat{\mathbf{x}}_i - \mathbf{x}_i\|_2^2$.

To avoid degenerate average latents and to cover the slide, we add two small terms:

$$\text{Coverage: } \mathcal{L}_{\text{cover}} = \frac{1}{N} \sum_i \max(0, \tau - u(i)), \quad (1)$$

$$u(i) = \max_z p_z(i), \quad (2)$$

$$\text{Diversity: } \mathcal{L}_{\text{feat}} = \|\text{offdiag}(\text{Cov}(\mathbf{Z}))\|_F^2. \quad (3)$$

where $p_z(i)$ is attention probability of a latent code z on token i and τ is an adaptive-parameter, explained in detail in Sec. 8. The total pretraining loss is $\mathcal{L}_{\text{MAE}} = \mathcal{L}_{\text{rec}} + \lambda_{\text{cover}} \mathcal{L}_{\text{cover}} + \lambda_{\text{feat}} \mathcal{L}_{\text{feat}}$.

Sparse Token Merger. To reduce obvious local redundancy before sending the tile-level tokens to the resampler, we merge tile-level tokens using a lightweight module, STM. On a virtual 2D coordinate grid, STM uses a non-overlapping $s \times s$ window for merge. For each window g with index set \mathcal{S}_g , where the number of \mathcal{S}_g is determined by the window size: $g = u \cdot \lfloor r_i/s \rfloor + \lfloor c_i/s \rfloor$, where u is a large number to prevent hash collision. For each \mathcal{S}_g , we first

compute $\tilde{\mathbf{x}}_i = \text{LN}_{\text{in}}(\mathbf{x}_i)$, $i \in \mathcal{S}_g$ and merge them within \mathcal{S}_g :

$$\tilde{\mathbf{x}}_g = \text{LN}_{\text{out}}\left(\frac{1}{\sqrt{|\mathcal{S}_g|}} \sum_{i \in \mathcal{S}_g} \tilde{\mathbf{x}}_i\right), \quad \tilde{\mathbf{c}}_g = (\lfloor r_i/s \rfloor, \lfloor c_i/s \rfloor) \quad (4)$$

yielding $\tilde{\mathbf{X}} \in \mathbb{R}^{N' \times D_v}$ with $N' \approx N/s^2$ and merged coordinates $\tilde{\mathbf{C}}$. For training numerical stability while we use mixed precision, we empirically divide $\sqrt{|\mathcal{S}_g|}$ for each \mathcal{S}_g instead of $|\mathcal{S}_g|$. The demo computation procedure is shown in Fig. 3 (c).

3.2. Integrating Vision with LLM Efficiently

While our resampler (Sec. 3.1) reduces tile tokens to L latents, to avoid the costly fusion within LLM, we propose an efficient two-stage fusion mechanism. First, a 2-layer MLP projector aligns latents to the LLM space: $\mathbf{V} = \text{Proj}(\mathbf{Z}) \in \mathbb{R}^{L \times D}$, where D is the embedding dimension of LLM. Second, a lightweight Token Importance Scorer (TIS) dynamically selects the Top- M query-relevant latents ($M \leq L$). These are fed into our Cross-Attention Routing Adapters (CARA), which efficiently integrate them with the LLM at a cost of $O(TM)$, where T is the length of the text tokens.

Token Importance Scorer (TIS). To further mimic the human experts' focus on the different regions of WSI for a given query, we allow the query to attend to select the Top- M most salient visual latents ($M \leq L$). Concretely, we mean-pool the text tokens to $\tilde{\mathbf{q}} \in \mathbb{R}^D$ and compute query-conditioned scores: $\mathbf{a}_i = \text{GELU}(W_v \tilde{\mathbf{v}}_i + W_q \tilde{\mathbf{q}})$, $s_i = \mathbf{w}^\top \mathbf{a}_i$, where W_v, W_q, \mathbf{w} are learnable weights. We select the index set \mathcal{I} corresponding to the Top- M scores, where $|\mathcal{I}| = M$. To train TIS without extra labels, we use attention distillation from the CARA layers. Let \mathcal{L} be the set of decoder layers where CARA is inserted, and let H be the number of attention heads. At each layer $\ell \in \mathcal{L}$, CARA performs text \rightarrow vision cross-attention over the M selected latents \mathbf{Z}_M and yields attention weights $\alpha^{(\ell)} \in \mathbb{R}^{B \times H \times T \times M}$ (per batch, head, text position, and latent). We form a *per-latent teacher score* by averaging over heads and text positions and then aggregating across CARA layers: $a_{b,i} = \frac{1}{|\mathcal{L}|} \sum_{\ell \in \mathcal{L}} \left(\frac{1}{H} \sum_{h=1}^H \sum_{t=1}^T \alpha_{b,h,t,i}^{(\ell)} \right)$, where $i \in \mathcal{I}$, $b = 1, \dots, B$. We define the teacher distribution \mathbf{t} and student distribution \mathbf{p} over these selected latents: $t_{b,i} = \text{softmax}(a_{b,i}/\tau_t)$ and $p_{b,i} = \text{softmax}(s_{b,i}/\tau_s)$, where τ_t and τ_s are two temperature terms. The TIS loss is the batch-mean forward KL between teacher and student, computed only on the routed latents \mathcal{I} : $\mathcal{L}_{\text{TIS}} = \frac{1}{B} \sum_{b=1}^B \sum_{i \in \mathcal{I}} t_{b,i} (\log t_{b,i} - \log p_{b,i})$. To further stabilize training and enforce order consistency, we add a pairwise ranking loss, $\mathcal{L}_{\text{rank}}$, which encourages the scorer's ranking of tokens to align with the teacher's. The detailed formulation of $\mathcal{L}_{\text{rank}}$ is provided in Sec. 7.

Cross-Attention Routing Adapter (CARA). We integrate the selected latents $\mathbf{V}_{\mathcal{I}}$ into the LLM. Inspired by

Flamingo [1], we insert CARA into a small set of decoder layers \mathcal{L} . Given hidden states $\mathbf{H}^{(\ell)}$ at layer ℓ , CARA performs gated cross-attention: $\tilde{\mathbf{H}}^{(\ell)} = \mathbf{H}^{(\ell)} + g_\ell \cdot \text{Attn}(\text{LN}(\mathbf{H}^{(\ell)}), \mathbf{V}_\mathcal{I}, \mathbf{V}_\mathcal{I})$ where g_ℓ is a learnable gate (initialized small) to stabilize early training. Then, the modality integration loss, with the standard auto-regressive loss \mathcal{L}_{LM} between the model output $\hat{\mathbf{Y}}$ and text label \mathbf{Y} can be written as

$$\mathcal{L} = \mathcal{L}_{\text{LM}} + \lambda_{\text{TIS}} \mathcal{L}_{\text{TIS}} + \lambda_{\text{rank}} \mathcal{L}_{\text{rank}}. \quad (5)$$

4. Experiment

4.1. Experimental Settings

Dataset. We use three distinct datasets to evaluate our design choices. The WSI-Bench dataset, introduced in WSI-LLaVA [27], is the primary source for training the resampler and for subsequent modality fusion with LLMs. It has over 9k WSIs and over 170k VQA pairs. For zero-shot testing, we assess the trained models on the WSI-Bench test set, as well as on Slide-Bench from SlideChat [9] and selected data from Path-Bench [46]. Notably, Slide-Bench contains BCNB WSIs [51], which differ from the TCGA WSIs [50] in WSI-Bench, making it an effective out-of-distribution (OOD) test set. As both WSI- and Path-Bench are based on the TCGA dataset, we remove any overlapping WSIs between WSI- and Path-Bench training sets. After this adjustment, we retain 400 WSIs and 780 visual question-answer pairs from the Path-Bench dataset. For the pre-processing, we first apply DSMIL [24] and CLAM [29] to identify tissue patches at 20 \times magnification and remove background regions. By using the CONCH V1 [32], we then extract tile-level features from these patches. The tile size is 224 \times 224. More details are provided in Sec. 8.

Experimental Details. The resampler is first pre-trained using MAE for 100k steps. After pre-training the resampler, we fuse the modality with the LLM in another two training stages. We use Qwen2.5-7B-Instruct [47] as the LLM to balance training cost and performance. The adapters are inserted to decoder layers {1, 3, 5, 7} in LLM. In the first fusion stage, we freeze the resampler and LLM, but with STM on and only train the projector, TIS, and CARA with $M = 96$. During this stage, we train the model using the report data in WSI-Bench [27]. In the second fusion stage, we use all the VQA pairs and unfreeze the latents and the last layer of the resampler. More details are in Sec. 8.

Baselines. To verify the effectiveness of our LoC-Path framework, we compare it with several end-to-end MLLMs, including GPT-4o [21], Quilt-LLaVA [41], WSI-LLaVA [27], and SlideChat [9]. The input tokens for SlideChat [9] are 20480. We resize the WSI thumbnails to 1024 \times 1024 for Quilt-LLaVA [41]. To compare with other token reduction methods, we compare Token Merge

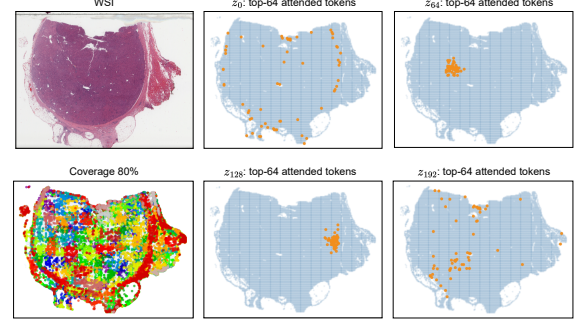


Figure 4. Coverage and visualization of latent attention preferences. The left bottom panel shows coverage: a token i is marked covered by any latent z if $\max_z p_{z,i} > \tau$; coverage = fraction of covered tokens ($\tau = 10^{-4}$). 80% coverage means the resampler attends to 80% of token positions on the slide. z_0 denotes the spatial locations of the top-64 input visual tokens receiving the highest attention score from the resampler’s latent z_0 . Orange points mark selected tokens; the blue background shows all token positions.

(ToMe) [5, 56], DivPrune [2], ACMIL [55], and the adaptive average pooling method. We replace our STM and the resampler with these token reduction methods, but leave the projector, TIS, and CARA components unchanged. We set the merged result token length to be 256 with $M = 96$. For ToMe, we use the balanced implementation from AIM [56], and we iteratively do tile-level token merge until the token length reaches 256. For ACMIL [55], we follow the attention head design and use the attention score to select 256 tile-level tokens. For DivPrune [2], we prune token length at different rates to reach the same 256 token length. We also train the token reduction baselines in two fusion stages.

Evaluation Metrics.

For the visual question answering (VQA) tasks, we follow the approach of WSI-LLaVA [27] and categorize the tasks into four types: morphological analysis, diagnosis, treatment planning, and report generation. For open-ended questions, we evaluate performance using BLEU [39], WSI-Precision, and WSI-Relevance, while accuracy is used for closed-ended tasks. WSI-Precision and WSI-Relevance are LLM-based evaluation metrics, proposed in WSI-LLaVA [27], with GPT-4o [21] serving as the evaluator. To assess the effectiveness of our resampler and the quality of the slide-level latent representations, we use AUC [17] and Accuracy [43] as the primary metrics for classification tasks. For the feature quality assessment from the resampler, we assess the latent attention coverage at $\tau=10^{-4}$ with $\mathbb{E}[\frac{1}{N} \sum_i \mathbf{1}\{\max_z p_z(i) > \tau\}]$, similar definition in Equ. 3 as well as the pairwise cosine similarity (diversity) between each latent code.

4.2. Results

Compressed Slide-level Representation from the Resampler. To verify the design of our resampler, we first com-

Table 1. Comprehensive comparison of our resampler with 256 latents and GigaPath’s slide-level encoder on classification performance, feature quality, and computational cost. Feature quality is measured on $2k$ WSIs sampled from the TCGA dataset based on the tumor type. Computational cost (including peak memory and TFLOPS) is measured during inference with a fixed input of $60k$ tokens.

Model	Subtype		Vital Analysis		Feature Quality (mean)		Computational Cost	
	AUC \uparrow	Acc \uparrow	AUC \uparrow	Acc \uparrow	Diversity (std) \downarrow	Coverage \uparrow	Mem (MB) \downarrow	TFLOPS \downarrow
Ours (no regularizer)	0.741	0.672	0.714	0.845	0.110 (0.462)	0.812	2254.5	1.713
Ours (MAE)	0.763	0.734	0.696	0.845	0.346 (0.056)	0.894	2254.5	1.713
Slide-level Encoder [52]	0.727	0.672	0.725	0.854	0.382 (0.197)	—	4022.2	10.340

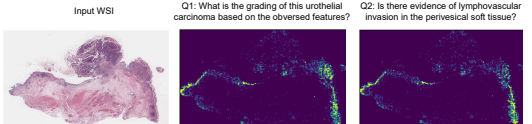


Figure 5. Query-aware visual tokens selection. Each heatmap shows the aggregated attention of the Top- M TIS-selected latents for a single WSI under two different queries. The brighter regions correspond to visual tokens that the TIS module deems most relevant to the query, illustrating how the model focuses on distinct morphological cues depending on the question.

Input WSI	
Question	What are the notable features of the cellular morphology in this slide?
Reference	The tumor cells display considerable nuclear pleomorphism with enlarged and irregularly shaped nuclei characteristic of poorly differentiated carcinoma. Some nuclear hyperchromasia is observed, alongside an increased mitotic area, indicating active cell division. The background shows signs of chronic inflammation and fibrosis.
Ours	The cellular morphology reveals significant nuclear pleomorphism, with marked variability in nuclear size and shape. The nuclei are irregularly shaped and hyperchromatic, indicating a high degree of atypia. There is also an increased mitotic rate, suggesting heightened proliferative activity within the tumor cells.

Figure 6. The quality comparison between our model and the reference answer. The same color indicates the matched claims between the model’s response and the reference.

pare it with the slide-level encoder on two classification tasks: sub-typing and vital analysis of BRCA tumor type. As shown in Tab. 1, our light-weight resampler with 256 latents achieves comparable AUC on both classification tasks compared to GigaPath [52]. To achieve such performance, our resampler only requires *half* the memory and $\approx 1/6$ of *FLOPs* compared to the slide-level encoder. For the feature quality, we mainly check resampler’s latent attention coverage and latent diversity, qualitatively shown in Fig. 4. In Tab. 1, latents from the resampler achieve similar diversity as GigaPath while maintaining low std across WSIs. For the coverage, the latents can cover over 80% input tokens. Two regularization terms further improve the attention coverage and keep the latents diverse. The details about the classification head implementation, and more comparisons of other pre-training methods are in Sec. 9.

The Overall Performance against Baselines. In Tab. 2, our framework outperforms all token reduction baselines and achieves comparable performance with other end-to-end MLLMs, especially WSI-LLaVA (ours 0.739 vs 0.754). In Tab. 3, although our method on Slide-Bench is a bit lower

than DivPrune and Avg. Pooling, our method achieves the highest WSI-P (0.384) and WSI-R (0.473) in the report generation task, even when comparing to WSI-LLaVA [27]. Although other conventional NLU metrics are lower than WSI-LLaVA [27], higher WSI-P and WSI-R have been shown to be more accurate and clinically relevant than conventional NLU metrics in pathological contexts [27]. Our model is the most computationally efficient in Tab. 2 due to the design of TIS and CARA modules. The inference TFLOPs of our model ($L=128/M=96$) are 81.91% lower than all the general baselines compared, and inference memory is also 38.9% lower. The qualitative comparison to the reference answer is shown in Fig. 6. More analysis are in Sec. 12.

Fusion Style Comparison. We compare fusion styles in Tab. 4 (b), fixing the resampler output to $L = 256$ latents and routing $m = 96$ tokens. Our CARA+TIS fusion method achieves the highest performance on WSI-Bench, Avg (0.738). The LLaVA-style fusion achieves the second highest WSI-Bench average (0.733). The standard Flamingo-style (no projector and only attention projection heads used in cross-attention adapters) baseline is slightly lower on the WSI-Bench average. Adding the TIS to the Flamingo-style adapters recovers performance. This comparison indicates that using projector to integrate vision features with LLM improves the overall performance like LLaVA-style and our CARA+TIS improves the performance compared to standard LLaVA-style fusion.

4.3. Ablation Study

Impact of the Latent Length in Resampler. We focus on the MLLM setting and vary the resampler’s latent length L while keeping the Top- M selected tokens active to capture language-side complexity. On WSI-Bench (except report generation), a *moderate* latent pool works best: $L=512$ with $M=384$ attains the highest average (0.741), compared to others in Tab. 4 (a). The trend indicates that increasing L initially improves retrieval of rare but relevant regions for the router, whereas overly large L introduces redundancy and dilutes attention. If we keep the M while increasing L , the performance decreases a little bit.

Impact of STM. On the *vision side*, using STM translates into large measured savings: with the same 60k-token input, adding STM with $s=4$ saves around $14 \times$ TFLOPs and $3.7 \times$

Table 2. Detailed performance and efficiency comparison on the WSI-Bench test set, categorized by task type. WSI-P and WSI-R denote WSI-Precision and WSI-Relevance, respectively, evaluated by GPT-4o [21]. Acc denotes Accuracy. Inference memory and TFLOPs are compared for all *General* ↓ (lower is better). Values are per single forward pass, reporting peak reserved memory usage (GB) and TFLOPs. We compare only the LLM generation cost (visual inputs are pre-extracted for SlideChat [9] and WSI-LLaVA [27]). LLMs loaded in 16-bit with SDPA attention and KV cache on; ours merges LoRA weights [19]. Percentages for **Ours** are reductions vs. the mean of *General*.

Model	Max Visual Token Number	Memory (GB) ↓	TFLOPs ↓	Morphological Analysis			Diagnosis			Treatment Planning			Average ↑
				Open		Close	Open		Close	Open		Close	
				WSI-P ↑	WSI-R ↑	Acc ↑	WSI-P ↑	WSI-R ↑	Acc ↑	WSI-P ↑	WSI-R ↑	Acc ↑	
<i>General:</i>													
GPT-4o [21]	-	-	-	0.220	0.204	0.471	0.472	0.457	0.530	0.496	0.841	0.875	0.507
Quilt-LLaVA [41]	576	12.620	12.798	0.448	0.447	0.947	0.586	0.604	0.849	0.788	0.816	1.000	0.721
SlideChat [9]	20480	11.583	26.767	0.269	0.281	0.870	0.319	0.385	0.767	0.654	0.577	0.333	0.495
WSI-LLaVA [27]	576	13.619	10.491	0.488	0.610	0.951	0.610	0.612	0.863	0.810	0.845	1.000	0.754
<i>Token Reduction:</i>													
ToMe (AIM) [56]	256	-	-	0.535	0.593	0.942	0.528	0.556	0.842	0.733	0.779	1.000	0.723
DivPrune [2]	256	-	-	0.527	0.581	0.921	0.491	0.515	0.820	0.518	0.627	0.854	0.650
ACMIL [55]	256	-	-	0.535	0.593	0.943	0.528	0.556	0.842	0.733	0.779	1.000	0.723
Avg. Pooling	256	-	-	0.532	0.593	0.940	0.545	0.574	0.845	0.666	0.766	0.958	0.713
Ours (L=256/M=96)	256	7.709	3.388	0.564	0.626	0.943	0.570	0.598	0.860	0.734	0.771	0.979	0.738
Ours (L=128/M=96)	128	7.709 (-38.9%)	3.019 (-81.91%)	0.567	0.620	0.931	0.582	0.613	0.849	0.733	0.769	1.000	0.739

Table 3. Combined results on WSI-Bench (report generation) and zero-shot generalization (Slide-Bench and Path-Bench subset). Rows under *General* are general-purpose MLLMs; rows under *Token Reduction* apply token compression.

Model	WSI-Bench: Report Generation						Zero-shot Generalization		
	BLEU-1 ↑	BLEU-2 ↑	ROUGE-L ↑	METEOR ↑	WSI-P ↑	WSI-R ↑	Slide-Bench Acc ↑	Path-Bench Acc ↑	
<i>General:</i>									
GPT-4o [21]	0.202	0.069	0.132	0.167	0.067	0.138	0.414		0.793
Quilt-LLaVA [41]	0.474	0.351	0.475	0.460	0.324	0.333	0.163		0.380
SlideChat [9]	0.439	0.107	0.161	0.137	0.123	0.168	0.546		0.847
WSI-LLaVA [27]	0.480	0.358	0.490	0.465	0.380	0.429	0.553		0.690
<i>Token Reduction:</i>									
ToMe (AIM) [56]	0.586	0.309	0.384	0.418	0.377	0.469	0.508		0.820
DivPrune [2]	0.556	0.286	0.375	0.417	0.335	0.419	0.544		0.737
ACMIL [55]	0.572	0.294	0.374	0.401	0.334	0.422	0.508		0.821
Avg. Pooling	0.569	0.296	0.372	0.406	0.320	0.423	0.545		0.837
Ours (L=256/M=96)	0.579	0.312	0.390	0.426	0.369	0.462	0.519		0.813
Ours (L=128/M=96)	0.583	0.313	0.392	0.425	0.384	0.473	0.519		0.847

Table 4. Ablation results on latent length sweep and different modality fusion strategies. WSI-Bench (except report generation) reports the average score (↑). For the ablation on fusion style, L and M are fixed at 256 and 96, respectively. Full per-task results are provided in Sec. 11.

(a) Latent length sweep		(b) Fusion style	
L / M	WSI-Bench Avg	Fusion	WSI-Bench Avg
128 / 96	0.739	LLaVA	0.733
256 / 96	0.738	Flamingo	0.726
256 / 144	0.729	Flamingo + TIS	0.729
512 / 384	0.741	Ours w.o. TIS	0.736
1024 / 576	0.731	Ours	0.738

Table 5. STM impact on vision cost (TFLOPs, Memory) vs. final MLLM performance (WSI-Bench Avg).

Setting	s	TFLOPs ↓	Mem (MB) ↓	WSI-Bench Avg ↑
No Merge	0	1.713	2254.5	0.735
Merge 2x	2	0.440	704.5	0.738
Merge 4x	4	0.121	607.1	0.737

memory reduction relative to the resampler-only setting, without much performance decrease, shown in Tab. 5. Also, the averaged score with $s=2$ slightly exceeds the no-merge setting, with per-task changes mostly within ± 0.02 . Taken

together with the large compute savings above, STM offers a favorable accuracy–efficiency trade-off.

Impact of TIS. The effectiveness of TIS is shown in two comparisons, in Tab. 4 (b). First, comparing our full model to an ablation without it, the inclusion of TIS provides a clear performance gain of 0.002. Second, to isolate its effect further, we added TIS to a standard “Flamingo” style fusion. The result shows the same positive trend: “Flamingo + TIS” outperforms the standard “Flamingo” baseline by 0.003 margin. In both contexts, the TIS consistently improves the model’s average score. This demonstrates that dynamically routing only the most salient visual information, as guided by the TIS, qualitatively shown in Fig. 5, is effective to help the LLM focus and improves performance.

5. Discussion and Conclusion

In this work, we addressed the computational inefficiency of applying multimodal large language models (MLLMs) to gigapixel-scale WSIs by leveraging their inherent data redundancy. We quantitatively demonstrate that this redundancy, both local and global, aligns with the sparse diagnostic process of human pathologists. We propose

the *LoC-Path* framework, featuring two redundancy-aware modules: a *Sparse Token Merger (STM)* to prune local redundancy and an *MAE-pretrained Resampler* to compress the global tile sequence. To efficiently fuse this representation, our novel *CARA+TIS* mechanism avoids quadratic complexity by restricting LLM attention to only the Top- M most salient visual latents, mimicking expert focus. Our extensive experiments demonstrate that our method achieves diagnostic performance comparable to that of state-of-the-art MLLMs while substantially reducing computational requirements (FLOPs) and memory demands. Crucially, beyond efficiency, the framework offers inherent interpretability through intermediate signals—such as STM merging grids, resampler attention maps, and TIS rankings—providing intuitive views of how the model allocates capacity across diagnostically relevant regions.

Limitations. Despite these gains, LoC-Path currently serves as an assisting tool rather than a standalone clinical system. First, the model relies on fixed pre-trained encoders; systematic biases or domain shifts (e.g., rare tumor subtypes) in the feature extractor inevitably propagate to the LLM. Second, while effective for global patterns, our compression prioritizes coverage over worst-case preservation, potentially under-representing subtle but decision-critical lesions. Consequently, as shown in our qualitative analysis in Sec. 12, the model struggles with fine-grained precision in complex tasks: it may hallucinate specific attributes (e.g., exact Nottingham scores) in report generation or offer generic rather than patient-specific regimens in treatment planning. Finally, current automatic metrics (e.g., WSI-Precision) may overestimate reliability by failing to penalize clinically dangerous hallucinations.

Future Research Directions. To bridge the gap between a reference tool and a hospital-deployable system, future work will focus on several key areas. First, we aim to extend the resampler’s MAE pre-training to handle diverse data granularities simultaneously, unifying patch-level and slide-level pathology data to learn more robust, multi-scale representations. Second, regarding modality fusion, we will explore broader possibilities for the CARA+TIS module, investigating diverse fusion modes to better integrate compressed visual signals with language logic. Furthermore, to improve report generation fidelity and treatment planning details, we plan to scale up training data and switch to more powerful LLM backbones, while integrating structured supervision—such as clinical guidelines and genomics—to reduce hallucinations. Finally, rigorous human evaluation and uncertainty estimation are essential to validate LoC-Path’s safety for real-world clinical deployment.

References

- [1] Jean-Baptiste Alayrac, Jeff Donahue, Pauline Luc, Antoine Miech, Iain Barr, Yana Hasson, Karel Lenc, Arthur Mensch, Katherine Millican, Malcolm Reynolds, Roman Ring, Eliza Rutherford, Serkan Cabi, Tengda Han, Zhitao Gong, Sina Samangoeei, Marianne Monteiro, Jacob Menick, Sebastian Borgeaud, Andrew Brock, Aida Nematzadeh, Sahand Sharifzadeh, Mikolaj Binkowski, Ricardo Barreira, Oriol Vinyals, Andrew Zisserman, and Karen Simonyan. Flamingo: a visual language model for few-shot learning. In *NeurIPS*, 2022. [1](#), [3](#), [4](#), [6](#)
- [2] Saeed Ranjbar Alvar, Gursimran Singh, Mohammad Akbari, and Yong Zhang. Divprune: Diversity-based visual token pruning for large multimodal models. In *CVPR*, 2025. [3](#), [6](#), [8](#)
- [3] Rohan Bareja, Francisco Carrillo-Perez, Yuanning Zheng, Marija Pizurica, Tarak Nath Nandi, Jeanne Shen, Ravi Maduri, and Olivier Gevaert. Evaluating vision and pathology foundation models for computational pathology: A comprehensive benchmark study. *medRxiv*, 2025. [3](#)
- [4] Mohsin Bilal, Manahil Raza, Youssef Altherwy, Anas Al-suhaihani, Abdulrahman Abduljabbar, Fahdah Almarshad, Paul Golding, Nasir Rajpoot, et al. Foundation models in computational pathology: A review of challenges, opportunities, and impact. *arXiv preprint arXiv:2502.08333*, 2025. [3](#)
- [5] Daniel Bolya, Cheng-Yang Fu, Xiaoliang Dai, Peizhao Zhang, Christoph Feichtenhofer, and Judy Hoffman. Token merging: Your vit but faster. In *ICLR*, 2023. [3](#), [6](#)
- [6] Liang Chen, Haozhe Zhao, Tianyu Liu, Shuai Bai, Junyang Lin, Chang Zhou, and Baobao Chang. An image is worth 1/2 tokens after layer 2: Plug-and-play inference acceleration for large vision-language models. In *ECCV*, 2024. [3](#)
- [7] Richard J Chen, Tong Ding, Ming Y Lu, Drew FK Williamson, Guillaume Jaume, Andrew H Song, Bowen Chen, Andrew Zhang, Daniel Shao, Muhammad Shaban, et al. Towards a general-purpose foundation model for computational pathology. *Nature medicine*, 2024. [1](#)
- [8] Xinlei Chen, Saining Xie, and Kaiming He. An empirical study of training self-supervised vision transformers. In *ICCV*, 2021. [2](#), [3](#)
- [9] Ying Chen, Guoan Wang, Yuanfeng Ji, Yanjun Li, Jin Ye, Tianbin Li, Ming Hu, Rongshan Yu, Yu Qiao, and Junjun He. Slidechat: A large vision-language assistant for whole-slide pathology image understanding. In *CVPR*, 2025. [1](#), [3](#), [6](#), [8](#), [2](#)
- [10] XTuner Contributors. Xtuner: A toolkit for efficiently fine-tuning llm, 2023. [2](#)
- [11] Tri Dao. Flashattention-2: Faster attention with better parallelism and work partitioning. In *ICLR*, 2024. [2](#)
- [12] Mohamed Dhouib, Davide Buscaldi, Sonia Vanier, and Ayman Shabou. Pact: Pruning and clustering-based token reduction for faster visual language models. In *CVPR*, 2025. [4](#)
- [13] Jiayu Ding, Shuming Ma, Li Dong, Xingxing Zhang, Shao-han Huang, Wenhui Wang, and Furu Wei. Longnet: Scaling transformers to 1,000,000,000 tokens. In *ICLR*, 2023. [1](#), [2](#)
- [14] Tong Ding, Sophia J Wagner, Andrew H Song, Richard J Chen, Ming Y Lu, Andrew Zhang, Anurag J Vaidya, Guillaume Jaume, Muhammad Shaban, Ahrong Kim, et al. A multimodal whole-slide foundation model for pathology. *Nature medicine*, 2025. [1](#), [6](#)
- [15] Zeyu Gao, Kai He, Weiheng Su, Ines P Machado, William McGough, Mercedes Jimenez-Linan, Brian Rous, Chunbao Wang, Chengzu Li, Xiaobo Pang, et al. Alpaca: Adapting llama for pathology context analysis to enable slide-level question answering. *medRxiv*, 2025. [1](#)
- [16] Nauman Ullah Gilal, Rachida Zegour, Khaled Al-Thelaya, Erdener Özer, Marco Agus, Jens Schneider, and Sabri Boughorbel. Pathvilm-eval: Evaluation of open vision language models in histopathology. *Journal of Pathology Informatics*, 2025. [3](#)
- [17] James A Hanley and Barbara J McNeil. The meaning and use of the area under a receiver operating characteristic (roc) curve. *Radiology*, 1982. [6](#)
- [18] Kaiming He, Xinlei Chen, Saining Xie, Yanghao Li, Piotr Dollár, and Ross Girshick. Masked autoencoders are scalable vision learners. In *CVPR*, 2022. [2](#)
- [19] Edward J. Hu, Yelong Shen, Phillip Wallis, Zeyuan Allen-Zhu, Yuanzhi Li, Shean Wang, Lu Wang, and Weizhu Chen. Lora: Low-rank adaptation of large language models. In *ICLR*, 2022. [8](#)
- [20] Wenxuan Huang, Zijie Zhai, Yunhang Shen, Shaosheng Cao, Fei Zhao, Xiangfeng Xu, Zheyu Ye, and Shaohui Lin. Dynamic-LLaVA: Efficient multimodal large language models via dynamic vision-language context sparsification. In *ICLR*, 2025. [4](#)
- [21] Aaron Hurst, Adam Lerer, Adam P Goucher, Adam Perelman, Aditya Ramesh, Aidan Clark, AJ Ostrow, Akila Welihinda, Alan Hayes, Alec Radford, et al. Gpt-4o system card. *arXiv preprint arXiv:2410.21276*, 2024. [6](#), [8](#)
- [22] Maximilian Ilse, Jakub Tomczak, and Max Welling. Attention-based deep multiple instance learning. In *ICML*, 2018. [2](#)
- [23] Sangwook Kim, Soonyoung Lee, and Jongseong Jang. Chatextaonepath: An expert-level multimodal large language model for histopathology using whole slide images. *arXiv preprint arXiv:2504.13023*, 2025. [3](#)
- [24] Bin Li, Yin Li, and Kevin W Eliceiri. Dual-stream multiple instance learning network for whole slide image classification with self-supervised contrastive learning. In *CVPR*, 2021. [1](#), [6](#)
- [25] Dong Li, Guihong Wan, Xintao Wu, Xinyu Wu, Xiaohui Chen, Yi He, Christine G Lian, Peter K Sorger, Yevgeniy R Semenov, and Chen Zhao. Multi-modal foundation models for computational pathology: A survey. *arXiv preprint arXiv:2503.09091*, 2025. [3](#)
- [26] Junnan Li, Dongxu Li, Silvio Savarese, and Steven Hoi. BLIP-2: bootstrapping language-image pre-training with frozen image encoders and large language models. In *ICML*, 2023. [1](#), [3](#)
- [27] Yuci Liang, Xinheng Lyu, Meidan Ding, Wenting Chen, Jipeng Zhang, Xiangjian He, Song Wu, Xiaohan Xing, Sen Yang, Xiyue Wang, and Linlin Shen. Wsi-llava: A multi-

- modal large language model for whole slide image. In *ICCV*, 2025. 1, 3, 6, 7, 8
- [28] Haotian Liu, Chunyuan Li, Qingyang Wu, and Yong Jae Lee. Visual instruction tuning. In *NeurIPS*, 2023. 1, 2, 3, 4
- [29] Ming Y Lu, Drew FK Williamson, Tiffany Y Chen, Richard J Chen, Matteo Barbieri, and Faisal Mahmood. Data-efficient and weakly supervised computational pathology on whole-slide images. *Nature biomedical engineering*, 2021. 1, 6
- [30] Ming Y Lu, Bowen Chen, Drew FK Williamson, Richard J Chen, Kenji Ikamura, Georg Gerber, Ivy Liang, Long Phi Le, Tong Ding, Anil V Parwani, et al. A foundational multimodal vision language ai assistant for human pathology. *arXiv preprint arXiv:2312.07814*, 2023. 3
- [31] Ming Y. Lu, Bowen Chen, Andrew Zhang, Drew F. K. Williamson, Richard J. Chen, Tong Ding, Long Phi Le, Yung-Sung Chuang, and Faisal Mahmood. Visual language pretrained multiple instance zero-shot transfer for histopathology images. In *CVPR*, 2023. 3
- [32] Ming Y Lu, Bowen Chen, Drew FK Williamson, Richard J Chen, Ivy Liang, Tong Ding, Guillaume Jaume, Igor Odintsov, Long Phi Le, Georg Gerber, et al. A visual-language foundation model for computational pathology. *Nature medicine*, 2024. 1, 2, 6, 3, 5
- [33] Ming Y Lu, Bowen Chen, Drew FK Williamson, Richard J Chen, Ivy Liang, Tong Ding, Guillaume Jaume, Igor Odintsov, Long Phi Le, Georg Gerber, et al. A visual-language foundation model for computational pathology. *Nature medicine*, 2024. 3
- [34] Ming Y Lu, Bowen Chen, Drew FK Williamson, Richard J Chen, Melissa Zhao, Aaron K Chow, Kenji Ikemura, Ahrong Kim, Dimitra Pouli, Ankush Patel, et al. A multimodal generative ai copilot for human pathology. *Nature*, 2024. 3
- [35] Weimin Lyu, Qingqiao Hu, Kehan Qi, Zhan Shi, Wentao Huang, Saumya Gupta, and Chao Chen. Efficient whole slide pathology vqa via token compression. *arXiv preprint arXiv:2507.14497*, 2025. 1
- [36] Xinheng Lyu, Yuci Liang, Wenting Chen, Meidan Ding, Jiaqi Yang, Guolin Huang, Daokun Zhang, Xiangjian He, and Linlin Shen. Wsi-agents: A collaborative multi-agent system for multi-modal whole slide image analysis. *arXiv preprint arXiv:2507.14680*, 2025. 3
- [37] Antoine Miech, Jean-Baptiste Zhukov, Jean-Baptiste Alayrac, Makarand Tapaswi, Ivan Laptev, and Josef Sivic. End-to-end learning of visual representations from uncurated instructional videos. In *CVPR*, 2020. 2, 3
- [38] Maxime Oquab, Timothée Darcret, Théo Moutakanni, Huy Vo, Marc Szafraniec, Vasil Khalidov, Pierre Fernandez, Haziza Daniel, Babilksa Adina, Nicolas Bordenave, et al. Divenov2: Learning robust visual features without supervision. *Transactions on Machine Learning Research*, 2024. 6
- [39] Kishore Papineni, Salim Roukos, Todd Ward, and Wei-Jing Zhu. Bleu: A method for automatic evaluation of machine translation. In *ACL*, 2002. 6
- [40] Jeff Rasley, Samyam Rajbhandari, Olatunji Ruwase, and Yuxiong He. Deepspeed: System optimizations enable training deep learning models with over 100 billion parameters. In *KDD*, 2020. 2
- [41] Mehmet Saygin Seyfioglu, Wisdom O Ikezogwo, Fatemeh Ghezloo, Ranjay Krishna, and Linda Shapiro. Quilt-llava: Visual instruction tuning by extracting localized narratives from open-source histopathology videos. In *CVPR*, 2024. 6, 8
- [42] Yuzhang Shang, Mu Cai, Bingxin Xu, Yong Jae Lee, and Yan Yan. Llava-prumerge: Adaptive token reduction for efficient large multimodal models. In *ICCV*, 2025. 3
- [43] David G Stork, Richard O Duda, Peter E Hart, and D Stork. Pattern classification. *A Wiley-Interscience Publication*, 2001. 6
- [44] Yuxuan Sun, Yixuan Si, Chenglu Zhu, Xuan Gong, Kai Zhang, Pingyi Chen, Ye Zhang, Zhongyi Shui, Tao Lin, and Lin Yang. Cpath-omni: A unified multimodal foundation model for patch and whole slide image analysis in computational pathology. In *CVPR*, 2025. 3
- [45] Yuxuan Sun, Yixuan Si, Chenglu Zhu, Kai Zhang, Zhongyi Shui, Bowen Ding, Tao Lin, and Lin Yang. Cpathagent: An agent-based foundation model for interpretable high-resolution pathology image analysis mimicking pathologists' diagnostic logic. *arXiv preprint arXiv:2505.20510*, 2025. 3
- [46] Yuxuan Sun, Hao Wu, Chenglu Zhu, Yixuan Si, Qizi Chen, Yunlong Zhang, Kai Zhang, Jingxiong Li, Jiatong Cai, Yuhang Wang, Lin Sun, Tao Lin, and Lin Yang. Pathbench: Advancing the benchmark of large multimodal models for pathology image understanding at patch and whole slide level. *IEEE Transactions on Medical Imaging*, 2025. 6
- [47] Qwen Team. Qwen2.5: A party of foundation models, 2024. 6
- [48] Eugene Vorontsov, Aican Bozkurt, Adam Casson, George Shaikovski, Michal Zelechowski, Kristen Severson, Eric Zimmermann, James Hall, Neil Tenenholz, Nicolo Fusi, et al. A foundation model for clinical-grade computational pathology and rare cancers detection. *Nature medicine*, 2024. 1
- [49] Peng Wang, Shuai Bai, Sinan Tan, Shijie Wang, Zhihao Fan, Jinze Bai, Keqin Chen, Xuejing Liu, Jialin Wang, Wenbin Ge, Yang Fan, Kai Dang, Mengfei Du, Xuancheng Ren, Rui Men, Dayiheng Liu, Chang Zhou, Jingren Zhou, and Junyang Lin. Qwen2-vl: Enhancing vision-language model's perception of the world at any resolution. *arXiv preprint arXiv:2409.12191*, 2024. 3, 4
- [50] John N Weinstein, Eric A Collisson, Gordon B Mills, Kenna R Shaw, Brad A Ozenberger, Kyle Ellrott, Ilya Shmulevich, Chris Sander, and Joshua M Stuart. The cancer genome atlas pan-cancer analysis project. *Nature genetics*, 2013. 2, 5, 6
- [51] Feng Xu, Chuang Zhu, Wenqi Tang, Ying Wang, Yu Zhang, Jie Li, Hongchuan Jiang, Zhongyue Shi, Jun Liu, and Mulan Jin. Predicting axillary lymph node metastasis in early breast cancer using deep learning on primary tumor biopsy slides. *Frontiers in Oncology*, 2021. 6, 2
- [52] Hanwen Xu, Naoto Usuyama, Jaspreet Bagga, Sheng Zhang, Rajesh Rao, Tristan Naumann, Cliff Wong, Zelalem Gero, Javier González, Yu Gu, Yanbo Xu, Mu Wei, Wenhui Wang, Shuming Ma, Furu Wei, Jianwei Yang, Chunyuan Li, Jianfeng Gao, Jaylen Rosemon, Tucker Bower, Soohee Lee,

- Roshanthi Weerasinghe, Bill J. Wright, Ari Robicsek, Brian Piening, Carlo Bifulco, Sheng Wang, and Hoifung Poon. A whole-slide foundation model for digital pathology from real-world data. *Nature*, 2024. [1](#), [7](#), [2](#), [3](#)
- [53] Weihao Ye, Qiong Wu, Wenhao Lin, and Yiyi Zhou. Fit and prune: Fast and training-free visual token pruning for multi-modal large language models. In *AAAI*, 2025. [4](#)
- [54] Tianyu Yu, Zefan Wang, Chongyi Wang, Fuwei Huang, Wenshuo Ma, Zhihui He, Tianchi Cai, Weize Chen, Yuxiang Huang, Yuanqian Zhao, Bokai Xu, Junbo Cui, Yingjing Xu, Liqing Ruan, Luoyuan Zhang, Hanyu Liu, Jingkun Tang, Hongyuan Liu, Qining Guo, Wenhao Hu, Bingxiang He, Jie Zhou, Jie Cai, Ji Qi, Zonghao Guo, Chi Chen, Guoyang Zeng, Yuxuan Li, Ganqu Cui, Ning Ding, Xu Han, Yuan Yao, Zhiyuan Liu, and Maosong Sun. Minicpm-v 4.5: Cooking efficient mllms via architecture, data, and training recipe, 2025. [3](#), [4](#)
- [55] Yunlong Zhang, Honglin Li, Yunxuan Sun, Sunyi Zheng, Chenglu Zhu, and Lin Yang. Attention-challenging multiple instance learning for whole slide image classification. In *ECCV*, 2024. [1](#), [6](#), [8](#)
- [56] Yiwu Zhong, Zhuoming Liu, Yin Li, and Liwei Wang. Aim: Adaptive inference of multi-modal llms via token merging and pruning. In *ICCV*, 2025. [3](#), [6](#), [8](#)

LoC-Path: Learning to Compress for Pathology Multimodal Large Language Models

Supplementary Material

6. Redundancy and Task Relevance Analysis

We quantify how much of a WSI’s tile–token stream is redundant (globally and locally), and how many tokens are actually task–relevant to the textual supervision. Our analyses operate on pre–extracted tile embeddings and are computed *per slide* and then summarized across slides by mean and inter–quartile range (IQR).

For each slide, let $X = \{x_i\}_{i=1}^N \subset \mathbb{R}^{D_v}$ denote tile embeddings and \bar{x} their mean. We report slide–wise statistics and aggregate them across $\sim 2k$ TCGA WSIs. We first stratified sampled from the WSI-Bench’s data, and WSIs are pre-processed at $20\times$ magnification, features are extracted from CONCH-V1 [32].

Global Compression Redundancy. To quantitatively show that the tile-level tokens are compressible, we design the following experiments: For $K \in \{8, 16, \dots, 256\}$ we learn K prototypes $\{ce_k\}$ (K-means). We assign each x_i to $ce(x_i)$ and compute the *normalized* reconstruction error:

$$\text{nMSE}(K) = \frac{\frac{1}{N} \sum_{i=1}^N \|x_i - ce(x_i)\|_2^2}{\frac{1}{N} \sum_{i=1}^N \|x_i - \bar{x}\|_2^2}.$$

Per slide, we obtain a curve $K \mapsto \text{nMSE}(K)$; across slides, we show the mean and IQR, and annotate the elbow and the K achieving $\approx 50\%$ error reduction. As a result, in Fig. 1a, we show that a small K prototypes are enough to reconstruct the slide fairly well, indicating potential for compression.

Local Redundancy. To assess the similarity between one tile and its neighbors, we find its nearest spatial neighbors $x_{nn(i)}$ and evaluate cosine similarity. For thresholds $\tau \in \{0.90, 0.92, 0.94, 0.96, 0.98\}$ we report

$$r_\tau = \frac{1}{N} \sum_{i=1}^N \mathbf{1}[\cos(x_i, x_{nn(i)}) > \tau].$$

, where $N = 16$ in our experiment. We aggregate r_τ over slides by mean and IQR. A large fraction of tiles exceed high cosine thresholds with a neighbor, which indicates strong *local* redundancy as we show in Fig. 1b.

Global Pairwise Similarity. Is high similarity common beyond nearest neighbors? To answer this question, we sample up to $50k$ unordered tile pairs (x_i, x_j) per slide and build a cosine histogram aggregated over slides. The right-skewed histogram in Fig. 1c demonstrates the high global redundancy.

Task Relevance Sparsity. To assess how many tiles are actually supervised by the report (caption), we study the relations between tile-level tokens and the global report embedding. Let t be the slide’s text (report) embedding. We follow the method in WSI-LLaVA [27] to clean the report, leaving the morphological and diagnosis information. For each tile, we compute $s_i = \cos(x_i, t)$ and then sort tiles by s_i in descending order and form the cumulative share of the *positive* similarity mass,

$$F(p) = \frac{\sum_{i=1}^{\lfloor pN \rfloor} \max(s_i, 0)}{\sum_{i=1}^N \max(s_i, 0)}, \quad p \in [0, 1].$$

We plot mean/median/IQR of $F(p)$ over slides and report the token fractions needed to reach 50/80/90% of the positive mass (e.g., $\sim 7.7\%/\sim 22.8\%/\sim 35.2\%$). Only a minority of tokens align with the text supervision. This shows that most tokens are not task-relevant.

7. Pairwise Ranking Loss Details

As mentioned in Sec. 3.2, we add a pairwise ranking loss ($\mathcal{L}_{\text{rank}}$) to the TIS training objective to stabilize learning and enforce order consistency.

To compute this loss, we first sort the Top- M indices I according to the teacher distribution q , yielding I_{sorted} . We select $n = \min(M/2, N_{\text{pairs}})$ pairs, where N_{pairs} is a hyperparameter (e.g., 8). We define the “high” set $I_{\text{hi}} = I_{\text{sorted}}[:n]$ (the top n indices) and the “low” set $I_{\text{lo}} = I_{\text{sorted}}[M//2:M//2+n]$ (the first n indices from the bottom half).

We form a set of n matched pairs $\mathcal{P} = \{(i_k, j_k) \mid i_k \in I_{\text{hi}}, j_k \in I_{\text{lo}}, k = 1..n\}$, where pairs are matched by their rank (i.e., 1st-highest i_1 is paired with 1st-lowest j_1). The loss uses a margin γ and weights w_{ij} that emphasize pairs with larger teacher gaps (i.e., pairs the teacher is more confident about):

$$w_{ij} = \frac{\max(q_i - q_j, 0)}{\frac{1}{|\mathcal{P}|} \sum_{(i', j') \in \mathcal{P}} \max(q_{i'} - q_{j'}, 0)}, \quad (6)$$

$$\mathcal{L}_{\text{rank}} = \frac{1}{|\mathcal{P}|} \sum_{(i, j) \in \mathcal{P}} w_{ij} [\gamma - (s_i - s_j)]_+, \quad (7)$$

where $[\cdot]_+ = \max(\cdot, 0)$, and s_i denotes the raw (unnormalized) scores from the TIS.

8. Implementation and Training Details

Implementation Details. The resampler has 2 LongNet [13] context layers and 2 cross-attention lay-

ers with self-attention layers as we discussed in Sec. 3.2. The segment set used for dilation attention in two LongNet [13] layers is [1024, 2024, 4096]. The stride sets are [1, 2, 4] and [4, 8, 16]. Moreover, we enable the relative positional encoding within LongNet’s dilation attention to help context layers better capture the short-to-mid range context [13]. For the following cross-attention layers, we set $K = 128$ for the first cross-attention layer and $K = 64$ for the second cross-attention layer. The embedding dimension of the resampler is 512, and the attention head is 8 for both context layers and cross-attention layers. We use 2D Fourier positional encoding for the resampler’s cross-attention key values. Doing so can help us deal with the filtered (missing) coordinates in the tile-level sequence and save memory, compared to 2D sinusoidal positional encoding.

Classification Task Conversion Details. In feature quality comparison experiments, we demonstrate the feature quality of the latents from the resampler. We use two classification tasks using BRCA tumor types. The first vital analysis classification tasks mark survival as 1 and not as 0; the sub-typing tasks define the first stage as 1 while other labels as 0, with unknown stages removed. The classification task head is a simple attention-based classification head from ABMIL [22].

Training Details. The resampler is pre-trained for 100k iterations on CONCH-V1 [32] WSI features with a mini-batch size of 2 per GPU and gradient accumulation 4 on 4 RTX A6000 Ada GPUs (effective global batch size 32). We randomly mask 75% of the input tokens and optimize the MAE objective \mathcal{L}_{MAE} introduced in Sec. 3.1, with $\lambda_{\text{cover}} = 5 \times 10^{-4}$ for the coverage term $\mathcal{L}_{\text{cover}}$ and $\lambda_{\text{feat}} = 1 \times 10^{-3}$ for the diversity term $\mathcal{L}_{\text{feat}}$. We use AdamW with an initial learning rate 1×10^{-4} , a 3% warm-up phase, and a cosine learning-rate schedule. During this pre-training we gradually anneal the Top- K in the resampler cross-attention from (128, 64) to (64, 32) following a cosine schedule.

We then train the first fusion stage for 3 epochs with a global batch size of 512 (batch size 2 per GPU and gradient accumulation 64 on 4 GPUs) and an initial learning rate 1×10^{-4} . In this stage we freeze both the Qwen2.5-7B-Instruct LLM and the resampler, and only train the visual projector together with the CARA+TIS modules on top of the LLM. The training objective is the multimodal loss as defined in Sec. 3.2, where we set $\lambda_{\text{TIS}} = \lambda_{\text{rank}} = 0.02$ for the self-distillation (TIS) loss \mathcal{L}_{TIS} and the ranking loss $\mathcal{L}_{\text{rank}}$.

In the second fusion stage, we unfreeze the resampler’s last cross-attention layer and its latent in-projection, and insert LoRA modules (rank 128, $\alpha = 64$) into all linear layers of the LLM. We then train all unfrozen components on all VQA pairs in WSI-Bench for 2 epochs with a global batch size of 128 and an initial learning rate 2×10^{-5} , again using the same multimodal fusion loss with $\lambda_{\text{TIS}} = \lambda_{\text{rank}} = 0.02$.

Across all training stages, we use Xtuner [10] with DeepSpeed ZeRO-2 [40] and FlashAttention 2 [11] for efficient training; FA2 is applied to the LLM self-attention but not to the cross-attention layers. A cosine learning-rate scheduler is used in all stages, and all experiments are conducted on 4 RTX A6000 Ada GPUs.

Training Optimization. The pre-training requires about 10 hours. The first fusion stage takes about 1 hour. The second fusion stage requires about 8 hours to 9 hours.

During development of the core training pipeline, we observed that the primary bottleneck was not GPU computational capability, but the overhead of transferring data to the GPUs. In digital pathology, tile-level features are commonly stored in .pt or .h5 formats. While these formats are not a problem for training on one or two GPUs, they incur substantial I/O overhead at larger scales, causing the data loader to spend a significant amount of time waiting for data. To mitigate this issue, we convert all tile-level features and their corresponding coordinates into .npy files separately, which supports more efficient memory mapping and lightweight loading. Furthermore, we store the features in float16 format while keeping coordinates in float32 format, to further reduce both storage and I/O costs. Since we only use mixed-precision training throughout all stages of our pipeline, using features in float16 format is not an issue.

With file format conversion, we are able to load long sequences with very low I/O costs. Unlike the conventional tile-level data loader in digital pathology [9, 51], loading one data point in a single batch, we are able to load multiple tile-level sequences in a single batch simultaneously. To deal with sequences with different lengths, we pack these sequences into the same length (we pad sequences with different lengths to the same 60k lengths and load padded sequences with their corresponding padding masks). As a result, we can increase the batch size to more than one (e.g 4) on each GPU. Doing so allows us to reduce the data loading rounds if we set the max training epochs to be 2.

With these optimizations, the training time of the second fusion stage is reduced from more than a day to less than 9 hours on our system. We also observe 2-3 times training time reduction on other stages.

9. Resampler Pretraining Method Comparison

We have already shown the MAE-pretrained resampler’s output latent (feature) quality in Sec. 4.2 and it has achieved comparable quality compared to Gigapath’s slide-level encoder [52]. Here, we compare our pre-training strategy against other pre-training strategies. These methods include MIL-NCE pre-training method [37] using randomly sampled tile-level tokens and their caption (report) pairs, pre-training only using LLM’s auto-regressive loss (LLaVA-style fusion), and pre-training using MoCoV3 [8]. For MIL-

Table 6. **Comparison of resampler pre-training strategies.** We report AUC and Accuracy for BRCA tumor subtyping and vital analysis tasks. Latent quality is evaluated via Mean Pairwise Cosine and Union Coverage, calculated on 2k random samples from the WSI-Bench training set.

Encoder	Pre-training	Subtype		Vital Analysis		Feature Quality (mean)	
		AUC \uparrow	Acc \uparrow	AUC \uparrow	Acc \uparrow	Diversity (std) \downarrow	Coverage \uparrow
CONCH V1 [32]	MIL-NCE [37]	0.692	0.719	0.754	0.857	0.999 (3.0e-4)	0.065
	LLM-loss [28]	0.724	0.688	0.759	0.882	0.841 (0.049)	1.000
	MoCoV3 [8]	0.705	0.594	0.554	0.863	0.999 (4.1e-5)	0.288
	Ours (no regularizer)	0.741	0.672	0.714	0.845	0.110 (0.462)	0.812
	Ours (MAE)	0.763	0.734	0.696	0.845	0.346 (0.056)	0.894
Prov-GigaPath [52]	MAE (Slide-level)	0.727	0.672	0.725	0.854	0.382 (0.197)	—

NCE pre-training [37], on the vision side, during training, we randomly sample over 500 tile-level tokens; on the language side, we use the global embedding of cleaned reports in WSI-Bench [27]. For the text encoder, we use CONCH-V1 [32]’s corresponding text encoder. For the end-to-end LLM-loss pre-training, we follow the LLaVA-like first fusion stage pre-training by adding a two-layer projector between LLM and resampler [28]. For the MoCoV3 [8] pre-training method, we first create two different views by subsampling the same tile-level token sequence for two resampler instances. In Tab. 6, the MAE-pretrained resampler’s internal cross-attention exhibits a good diversity score and high attention coverage, as we have shown in Sec. 4.2. Furthermore, its output latents demonstrate strong orthogonality (average cosine similarity 0.35). This indicates that it genuinely samples broadly across the whole slide rather than simply averaging. It also achieves an AUC of 0.763 on the BRCA subtype task.

The pre-training methods using text-supervision, including MIL-NCE [37] and end-to-end LLM-loss [28], achieve much higher downstream AUC and Acc on the vital analysis task compared to those that do not. This suggests that the text supervision does help the resampler create the link between the input to the final diagnosis prediction. The MIL-NCE pretrained resampler has very low attention coverage, while producing very similar output latents (very poor diversity). This indicates that this pre-training method only encourages the resampler to pay attention to those tile-level tokens with relevant text supervision. It is problematic when it comes to more rare cases, such as answering questions regarding locally specific morphological features. The LLM-loss-pretrained resampler exhibits high attention coverage while having similar output latents (very poor diversity). Combining these two pieces of evidence indicates that this resampler just computes the average for the input tile-level tokens instead of picking the important ones that can represent the whole tile-level sequence. The MoCoV3 [8] pretrained resampler has low attention coverage with very similar output latents. Thus, the MAE pre-training method actually achieves our design goal: the resampler first glances the whole sequence (high attention coverage), and then each latent code looks at the distinct place on the tile-level tokens rather than computing an average.

Table 7. **Ablation of resampler architecture.** We evaluate the impact of latent length (L), cross-attention depth, and context layer type on BRCA subtype and vital analysis tasks (AUC/Accuracy). Unless otherwise specified, the default configuration uses $L = 256$, MAE pre-training, and regularization terms.

Resampler Config.	Sub-typing		Vital Analysis	
	AUC \uparrow	Acc \uparrow	AUC \uparrow	Acc \uparrow
Ours	0.763	0.734	0.696	0.845
w/o Reg. Loss	0.741	0.672	0.714	0.845
<i>Num. Latents:</i>				
$L=128$	0.800	0.688	0.720	0.826
$L=512$	0.739	0.672	0.662	0.789
$L=1024$	0.760	0.719	0.687	0.839
<i>Cross-Attn Depth:</i>				
3 Layers	0.764	0.688	0.750	0.845
<i>Context Layer:</i>				
Depth-wise Conv.	0.741	0.656	0.674	0.826

10. Complexity Analysis of CARA Impact

Let T be the textual prefix length, L the number of raw visual latents, and $M \leq L$ the latents fed to the LLM via cross-attention in n_{\times} decoder layers (out of n total). With KV caching, LLaVA treats vision tokens as part of the autoregressive sequence, leading to a prefilling cost $\mathcal{O}(n(T + L)^2)$. In contrast, our design performs self-attention only over text and uses text \rightarrow vision cross-attention, reducing prefilling to $\mathcal{O}(nT^2 + n_{\times}TM)$, i.e., quadratic only in text and linear in M instead of L .

During decoding, LLaVA’s per-step attention scales with the whole prefix ($T + L$), yielding a total cost $\mathcal{O}(nA(T + L) + nA^2)$ for A generated tokens. In our model, self-attention is unchanged while cross-attention is linear in M and independent of A on the key/value side, giving $\mathcal{O}(n(AT + A^2) + n_{\times}AM)$. Memory usage follows the same trend: LLaVA’s KV cache grows as $\mathcal{O}(nd(T + L + A))$, whereas ours is $\mathcal{O}(nd(T + A)) + \mathcal{O}(n_{\times}Md)$ with a constant visual term. The gains are most pronounced when L is large (e.g., WSI), since we replace the $\mathcal{O}(L)$ dependence with $\mathcal{O}(M)$ both in prefill compute and in decoding’s per-step cost.

Model	Morphological Analysis			Diagnosis			Treatment Planning			Average ↑
	WSI-P	WSI-R	Acc	WSI-P	WSI-R	Acc	WSI-P	WSI-R	Acc	
<i>Fusion Ablation</i>										
LLaVA	0.556	0.619	0.933	0.558	0.594	0.852	0.722	0.759	1.000	0.733
Flamingo	0.551	0.605	0.934	0.537	0.572	0.835	0.729	0.771	1.000	0.726
Flamingo + TIS	0.552	0.615	0.944	0.536	0.566	0.834	0.756	0.782	0.979	0.729
<i>Gating Ablation (7B)</i>										
TIS Off	0.561	0.614	0.935	0.571	0.603	0.845	0.716	0.783	1.000	0.736
<i>Adapter Insertion Layers (7B)</i>										
Adapter First	0.557	0.611	0.931	0.563	0.601	0.847	0.711	0.770	0.979	0.730
Adapter Layers 1/8/15/22	0.558	0.609	0.933	0.553	0.591	0.847	0.734	0.777	1.000	0.734
<i>Token Merging Ablation</i>										
No Merge	0.556	0.614	0.934	0.553	0.597	0.860	0.725	0.772	1.000	0.735
Merge Size 3	0.557	0.608	0.935	0.566	0.594	0.840	0.707	0.792	0.979	0.731
Merge Size 4	0.557	0.614	0.937	0.573	0.612	0.850	0.717	0.776	1.000	0.737
<i>Latent + Router Top-M</i>										
$L=256, M=144$	0.555	0.608	0.940	0.549	0.587	0.827	0.718	0.774	1.000	0.729
$L=512, M=384$	0.558	0.610	0.940	0.567	0.609	0.854	0.743	0.791	1.000	0.741
$L=1024, M=576$	0.556	0.613	0.940	0.545	0.580	0.842	0.738	0.784	0.979	0.731

Table 8. **Detailed ablation results on WSI-Bench (7B LoC-Path).** This table expands upon the study in Sec. 4.3 of the main paper. Metrics include open-ended WSI-Precision (WSI-P), WSI-Relevance (WSI-R), and closed-ended Accuracy (Acc) across morphological, diagnostic, and treatment planning tasks. Best results within each ablation group are highlighted in **bold**.

Variant	Morphological Analysis			Diagnosis			Treatment Planning			Avg. ↑
	WSI-P	WSI-R	Acc	WSI-P	WSI-R	Acc	WSI-P	WSI-R	Acc	
<i>LLM Scale (CONCH-VI, STM+Resampler)</i>										
LoC-Path-7B ($L=256, M=96$)	0.564	0.626	0.943	0.570	0.598	0.860	0.734	0.771	0.979	0.738
LoC-Path-14B ($L=256, M=96$)	0.557	0.612	0.937	0.569	0.600	0.849	0.759	0.816	1.000	0.744
<i>Adapter Insertion</i>										
Adapter at Layer 1	0.557	0.611	0.931	0.563	0.601	0.847	0.711	0.770	0.979	0.730
Adapters at Layers 1/8/15/22	0.558	0.609	0.933	0.553	0.591	0.847	0.734	0.777	1.000	0.734
<i>CARA Gating and Ranking Loss</i>										
w/o CARA gating ($g_\ell=1$)	0.559	0.613	0.928	0.552	0.595	0.852	0.741	0.784	1.000	0.736
w/o TIS ranking loss	0.555	0.612	0.934	0.564	0.596	0.832	0.721	0.755	0.979	0.728
<i>Tile-level Encoder</i>										
DINOv2, $D_v = 768, 3 \times \text{CA}$	0.454	0.484	0.898	0.418	0.472	0.809	0.665	0.635	0.917	0.639
CONCH-V15, $D_v = 768, 3 \times \text{CA}$	0.559	0.619	0.938	0.562	0.610	0.865	0.744	0.805	1.000	0.745
<i>Top-K Attention in Resampler</i>										
Dense resampler (w/o Top-K)	0.511	0.579	0.916	0.470	0.505	0.739	0.621	0.696	0.854	0.655

Table 9. **Extended ablation studies.** We analyze the impact of LLM scale, adapter placement, CARA gating/ranking, tile-level encoders, and resampler attention patterns. Default configuration: 7B LLM, CONCH-V1 encoder, and a 512-dim resampler with two cross-attention layers. Scores represent WSI-Bench performance on non-report-generation tasks. For the LLM scale ablation, the 14B variant uses Qwen2.5-14B-Instruct as the LLM. For adapter insertion, we vary the decoder layers where CARA is added. For CARA gating, we disable the learnable gate by fixing $g_\ell=1$. For tile-level encoder ablations, we use CONCH-V1.5 and DINOv2, each with a 768-d resampler and three cross-attention layers. For the resampler ablation, the dense variant replaces the default Top-K cross-attention with dense attention.

This theoretical analysis aligns with our empirical results in Tab. 2 of the main paper, where we observe an over 70% reduction in FLOPs and $\approx 38\%$ savings in peak memory compared to standard LLaVA baselines [28].

11. More Ablation Study

Ablation of resampler architecture. Tab. 7 summarizes several design choices for the MAE-pretrained resampler

on the BRCA subtype and vital-analysis classification tasks. Adding the coverage and diversity regularizers improves the subtype AUC from 0.741 to 0.763 and also stabilizes training, while keeping vital-analysis performance unchanged. Varying the number of latents shows that moderate compression works best: $L=128$ achieves the highest subtype AUC but slightly worse vital-analysis accuracy, whereas very long latent sets ($L=512$ or 1024) underperform on both

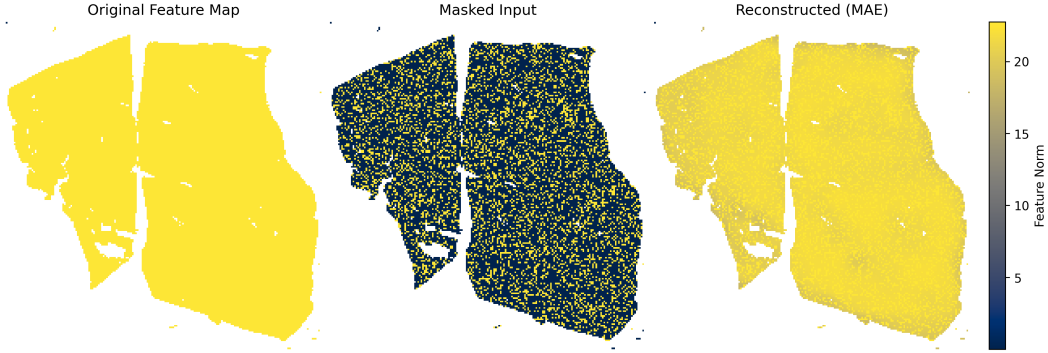


Figure 7. Visualization of MAE resampler reconstruction. Left: Original tile-level feature map (visualized by feature norm). Middle: Masked input (75% mask ratio); black regions indicate missing tokens. Right: Features reconstructed by the MAE-pretrained resampler (256 latents). Despite heavy corruption, the model successfully recovers the global tissue layout and feature magnitude, demonstrating the efficacy of the compressed latent representation.

tasks. Using three cross-attention layers improves both subtype and vital-analysis AUCs compared to the default two-layer design, but at a higher computational cost; our default strikes a balance between accuracy and efficiency. Finally, replacing the LongNet-style context layers with depth-wise convolutions noticeably hurts performance, confirming the importance of long-range context modeling before resampling.

Detailed WSI-Bench Ablations. Tab. 8 reports full per-task results on WSI-Bench (except report generation task) corresponding to the ablations in Sec. 4.3 of the main paper.

Impact of Top- K Attention in the Resampler. We further study whether the sparse Top- K cross-attention used in the resampler is necessary. To this end, we replace the Top- K operator with dense cross-attention while keeping all other components fixed (7B LLM, CONCH-V1 input tile-level tokens [32], STM, $L=256$ latents and $M=96$ selected tokens). As reported in Tab. 9, this dense resampler substantially hurts the WSI-Bench performance: the overall average drops from 0.738 (LoC-Path-7B with Top- K) to 0.655. The degradation is consistent across all three subtype tasks. These results confirm that enforcing sparsity via Top- K attention is crucial for learning diverse, coverage-aware latents that support strong slide-level reasoning.

Impact of TIS Ranking Loss. The new experiments in Tab. 9 isolate the effect of the ranking loss used to train the TIS. Removing the pairwise ranking loss while keeping the distillation loss leads to a noticeable drop in WSI-Bench average from 0.739 to 0.728. Most of the degradation comes from diagnosis and treatment-planning questions: the closed-form diagnosis accuracy decreases from 0.849 to 0.832, and treatment-planning obtains lower WSI-P/WSI-R. These results suggest that the ranking loss helps TIS produce a more stable and well-ordered importance distribution over latents, which in turn improves cross-layer

consistency of the routed tokens.

Impact of CARA Insertion Layers. To study where to insert CARA modules inside LLM, we compare placing only one CARA module in the LLM’s layer index 1 (“Adapter at Layer 1”) with distributing them across layers at index $\{1, 8, 15, 22\}$, as reported in Tab. 8. Both variants use the same visual configuration ($L=256$, $M=96$), but the distributed design achieves a higher WSI-Bench average (0.734 vs. 0.730). This indicates that injecting visual information at multiple depths allows the LLM to refine its reasoning with fresh slide-level evidence, rather than relying solely on early-layer fusion. However, when it compares to our default settings (inserting the CARA at LLM decoder layer index $\{1, 3, 5, 7\}$), distributed insertion gives slightly decreased performance. This might be caused by the fact that the deep decoder layers of LLM do not pay attention to the visual information, unlike the early layers.

Impact of the Gating Mechanism. Our CARA modules include a learnable scalar gate g_ℓ that controls how much visual information is injected at each decoder layer. In Tab. 8, turning off the gate (“TIS Off”) slightly reduces the WSI-Bench average and harms open-ended WSI-P/WSI-R on diagnosis, even though all visual latents are still available to the LLM. The experiments in Tab. 9 show an even clearer trend: forcing $g_\ell=1$ for all layers reduces the WSI-Bench average from 0.744 to 0.736, with noticeable drops in WSI-Precision and WSI-Relevance for both diagnosis and treatment planning. Together, these results confirm that letting the model softly gate visual information is more effective than always fusing all latents, and it also saves computation by avoiding unnecessary cross-attention when the gate is small.

Impact of Tile-level Encoders. We primarily use CONCH-V1 [32] features (512 feature dimension) as tile-level inputs, but our framework is compatible with other tile-level

vision encoders. Tab. 6 already shows that the MAE-pretrained resampler produces high-quality latents from CONCH-V1 features [32], matching the slide-level encoder upper bound on classification tasks. To further test robustness, we swap the tile encoder to CONCH-V15 [14], whose feature dimension is 768. To accommodate this higher dimension, we increase the resampler hidden size to 768 and use three cross-attention layers. As summarized in Tab. 9, the CONCH-V15[14] variant improves all three WSI-Bench tasks and achieves the best overall average (0.745), especially boosting WSI-Relevance for diagnosis and treatment planning. This suggests that LoC-Path can directly benefit from advances in pathology foundation models without changing the overall MLLM architecture. We also swap the tile-level encoder to a Dino V2 [38] variant without feature alignment pre-training, which yields worse overall performance on WSI-Bench tasks. This suggests that the feature space alignment training is essential to bridging the vision encoders and the pre-trained LLMs.

Impact of LLM Scale. Finally, we scale the language backbone from Qwen2.5-7B-Instruct (used in the main paper) to Qwen2.5-14B while keeping the visual stack and routing modules fixed [47]. On WSI-Bench, the 7B model in the main paper reaches an average score of 0.739, whereas the 14B variant in Tab. 9 improves this to 0.744. The gains are consistent across morphological analysis, diagnosis, and treatment planning, indicating that our token-compression pipeline already supplies a strong visual representation even for a relatively small LLM. Scaling up the language model yields additional accuracy, but is less noticeable compared to the gain by switching to a better tile-level encoder.

12. More Qualitative Results

MAE Resampler Reconstruction. To better illustrate what the MAE-pretrained resampler learns, Fig. 7 visualizes an example WSI before and after reconstruction. The left panel shows the original tile-level feature map, with feature norms encoded as a heatmap over the 2D grid. The middle panel shows the masked input used during pretraining, where 75% of the tiles are randomly removed. The right panel presents the reconstruction from our resampler decoder. Despite the heavy corruption, the model successfully recovers the global tissue layout and the overall magnitude of tile features, supporting our assumption that a small set of latents can faithfully encode the slide-level representation. This qualitative result complements the quantitative comparison with the slide-level encoder in Tab. 7.

Latent Diversity and Coverage. To further analyze the behavior of the resampler latents, Fig. 10 visualizes the Top- K attention maps of multiple latents on the same WSI as we have shown in Fig. 4. In Fig. 10, different latents focus on distinct tissue regions and morphological patterns. At the

same time, they cover most of the slide, matching the high coverage reported in Sec. 4.2. Compared with the aggregate statistics in Fig. 10 and Tab. 7, this qualitative view confirms that the resampler indeed “glances” over the whole WSI and allocates different latents to complementary visual contexts rather than redundantly attending to the same locations.

STM Merged Grid Visualization. Fig. 8 provides a visual explanation of how STM removes local redundancy. In Fig. 8, the right panel shows the merged grid after applying STM with a local window ($s=2$). Although the number of tokens is significantly reduced, the merged tokens still form a dense coverage of the tissue region and preserve coarse anatomical structures. This visualization is consistent with the quantitative results in Tab. 7 and Tab. 5 in the main paper, where STM does not hurt accuracy while dramatically reducing FLOPs and memory on the vision side.

Task-level Successes and Failure Modes. Fig. 9 illustrates LoC-Path’s performance across four tasks in WSI-Bench. Regarding successes (top row), the model accurately identifies dominant tumor types and key morphological patterns, such as invasive ductal carcinoma, infiltrative growth, and nuclear pleomorphism. This alignment with expert reports confirms that our compression preserves clinically salient regions. However, failure modes exist (bottom row). In treatment planning, the model tends to offer generic guideline-based regimens while under-emphasizing case-specific constraints like biomarkers. Similarly, in report generation, while correctly identifying tumor type and grade, it occasionally hallucinates fine-grained attributes (e.g., Nottingham scores or microcalcifications). Overall, LoC-Path reliably captures coarse diagnostic intent but lacks precision for granular decision-critical details, which also aligns with the quantitative results before.

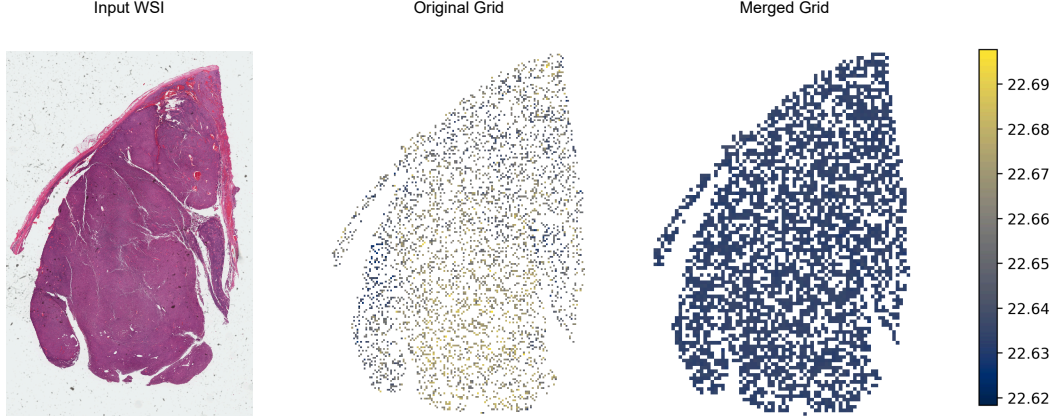


Figure 8. STM merging behavior on a TCGA WSI. From left to right: (i) input WSI thumbnail, (ii) original tile grid with per-tile feature norms, and (iii) merged grid after applying STM with a local window (e.g., $s=2$). STM aggressively reduces the number of tiles while largely preserving the overall tissue footprint and coarse morphology, illustrating how local redundancy can be removed before resampling.

Input WSI		Input WSI	
Question	Can you provide an overall description of the whole slide image?	Question	Based on the observation of the slide, what is the histological classification?
Reference	The whole slide image exhibits features of a poorly differentiated adenocarcinoma. The tissue demonstrates disorganized glandular structures with evidence of significant architectural distortion and nuclear atypia. The tumor extends beyond the prostate capsule, showing extracapsular extension into surrounding tissues. Extensive perineural invasion is visible, yet no angiolymphatic invasion is detected. Additionally, there is a presence of high-grade prostatic intraepithelial neoplasia, indicating precancerous changes.	Reference	The histological classification aligns with invasive ductal carcinoma. This classification is supported by the presence of poorly differentiated epithelial cells infiltrating the stroma with minimal glandular formation and significant deviation from the normal architecture observed in the slide.
Ours	The slide shows a disrupted architecture with malignant epithelial cells forming irregular glandular structures. These structures deviate significantly from the normal prostate tissue pattern, indicating an abnormal proliferation of glandular formations. The nuclei exhibit moderate variability in size and shape, suggesting some degree of nuclear atypia. There is also evidence of perineural invasion, where tumor cells are seen encircling or invading nerve fibers.	Ours	The histological classification based on the observed features is invasive ductal carcinoma. This is supported by the presence of poorly differentiated epithelial cells with minimal glandular formation, significant nuclear pleomorphism, and high mitotic activity.
Input WSI		Input WSI	
Question	What is the recommended treatment plan for a patient diagnosed with infiltrating ductal carcinoma, Nottingham grade II, TNM staging T2N0M0, and pending HER2 IHC results?	Question	What are the key features and diagnostic information that can be derived from the whole slide histopathology image?
Reference	1. Surgery: Perform breast-conserving surgery (lumpectomy) or mastectomy based on tumor characteristics and patient preference, along with sentinel lymph node biopsy. 2. Radiation Therapy: Consider adjuvant radiation therapy if breast-conserving surgery is performed. 3. Endocrine Therapy: If further testing indicates ER or PR positivity, prescribe tamoxifen or aromatase inhibitors for at least 5 years. 4. Chemotherapy: Pending HER2 results, consider adjuvant chemotherapy if further pathological risk factors are identified. 5. HER2-targeted Therapy: If HER2 positivity is confirmed, consider the addition of trastuzumab (Herceptin) with chemotherapy for HER2-targeted treatment.	Reference	Microscopic observation of the pathology slide reveals invasive carcinoma infiltrating the surrounding tissue. The histologic type is ductal, with the tumor cells forming irregular clusters and showing moderate deviation from normal architecture, corresponding to a histologic grade of 2. Nuclear features display moderate pleomorphism with variability in size and shape, resulting in a nuclear score of 3. Mitotic rate is high, with a mitotic score of 1. Vascular invasion is not identified, and no calcification is observed. The surrounding tissue includes ductal carcinoma in situ (DCIS) with a solid and cribriform pattern, moderate nuclear grade, and central necrosis. Based on these observations, the diagnosis is invasive ductal carcinoma, moderately differentiated, Nottingham Histologic Grade 2 (NHG2) with a total score of 7 out of 9.
Ours	1. Surgery: Consider breast-conserving surgery (lumpectomy) or mastectomy, depending on tumor size and patient preference, along with sentinel lymph node biopsy due to N0 status. 2. Chemotherapy: Recommend adjuvant chemotherapy if the HER2 IHC results are positive, given the potential for aggressive disease in HER2-positive cases. If HER2 is negative, consider chemotherapy based on additional risk factors such as age, tumor characteristics, and overall health. 3. Endocrine Therapy: Prescribe tamoxifen or aromatase inhibitors for at least 5 years if the tumor is hormone receptor-positive. 4. Radiation Therapy: Administer adjuvantly following breast-conservation surgery to reduce local recurrence risk.	Ours	Microscopic observation of the pathology slide reveals epithelial cells infiltrating the surrounding stroma with minimal formation of glandular structures, significantly deviating from normal tissue architecture. The nuclei exhibit moderate variability in size and shape, indicating nuclear pleomorphism. There is a moderate rate of cell division observed. Vascular invasion is not identified with this sample. Areas of ductal carcinoma in situ (DCIS) are present, displaying solid and cribriform patterns with central necrosis and microcalcifications. Based on these observations, the diagnosis is invasive ductal adenocarcinoma, Nottingham Histologic Grade 2 (NHG2), with a total score of 6 out of 9.

Figure 9. Qualitative success and failure cases across WSI-Bench tasks. Top row: Successful cases in morphological analysis and diagnosis, showing high overlap with expert descriptions. Bottom row: Typical failure modes in treatment planning and report generation. While the model captures global intent, it may miss targeted options or hallucinate details. (Red highlights indicate hallucinations or errors; Green highlights indicate correct key findings.)

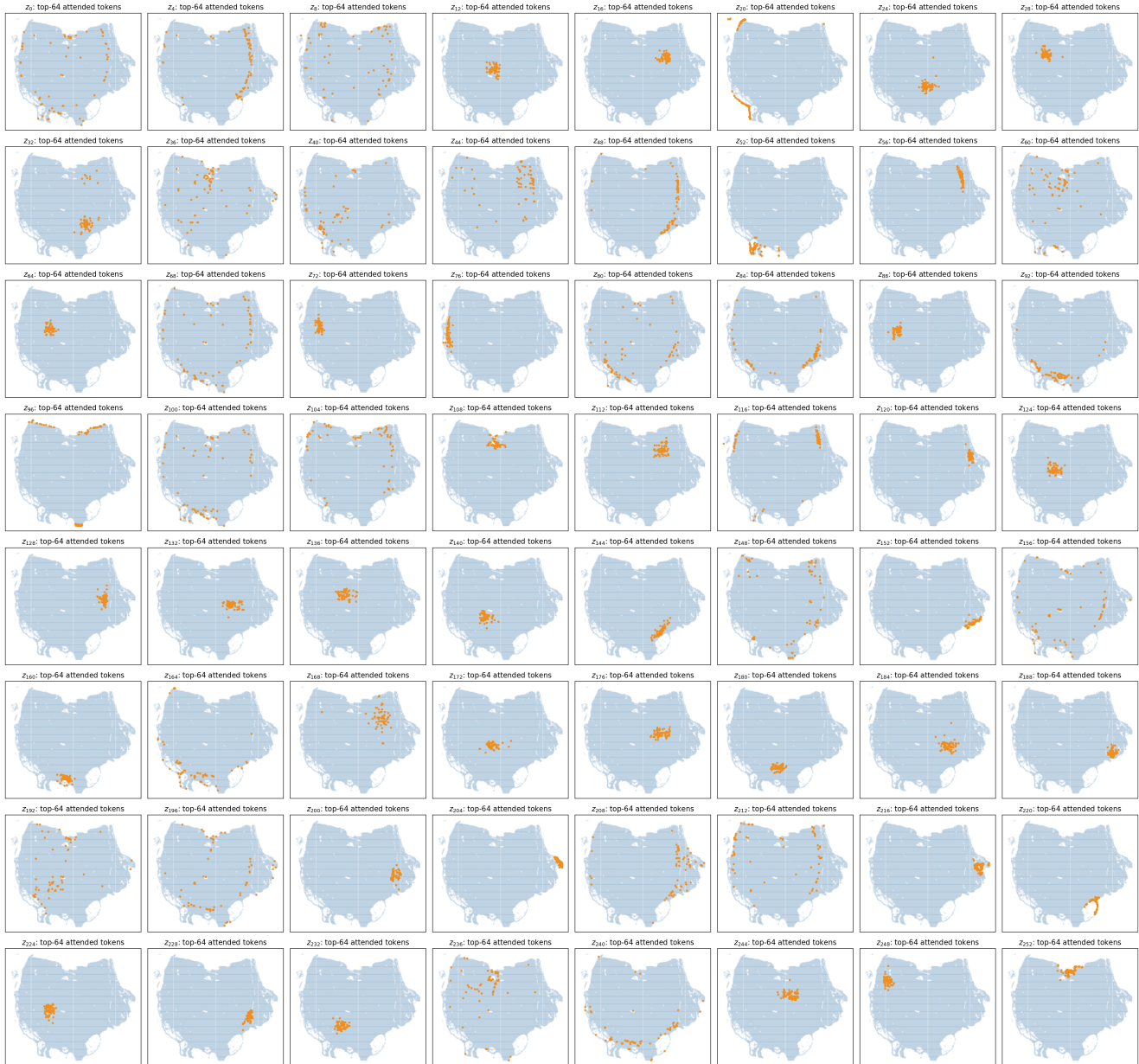


Figure 10. Diversity of resampler latents via Top- K attention. Each panel corresponds to one latent from the MAE-pretrained resampler. This resampler has 256 output latents. Orange dots mark the spatial locations of the Top-64 input tokens receiving the highest attention from that latent; the blue background shows all foreground token positions. Different latents specialize to distinct regions and structures while jointly covering the whole slide, qualitatively confirming the high coverage and diversity reported in Sec. 4.2 and Tab. 7.